

SHELS: OPTICAL SPECTRAL PROPERTIES OF WISE 22 μ M-SELECTED GALAXIES

HO SEONG HWANG¹, MARGARET J. GELLER¹, MICHAEL J. KURTZ¹, IAN P. DELL'ANTONIO², AND DANIEL G. FABRICANT¹

Last updated: August 16, 2012

ABSTRACT

We use a dense, complete redshift survey, the Smithsonian Hectospec Lensing Survey (SHELS), covering a 4 square degree region of a deep imaging survey, the Deep Lens Survey (DLS), to study the optical spectral properties of Wide-field Infrared Survey Explorer (*WISE*) 22 μ m-selected galaxies. Among 507 *WISE* 22 μ m-selected sources with $(S/N)_{22\mu m} \geq 3$ ($\approx S_{22\mu m} \gtrsim 2.5$ mJy), we identify the optical counterparts of 481 sources ($\sim 98\%$) at $R < 25.2$ in the very deep, DLS R -band source catalog. Among them, 337 galaxies at $R < 21$ have SHELS spectroscopic data. Most of these objects are at $z < 0.8$. The infrared (IR) luminosities are in the range $4.5 \times 10^8 (L_\odot) \lesssim L_{IR} \lesssim 5.4 \times 10^{12} (L_\odot)$. Most 22 μ m-selected galaxies are dusty star-forming galaxies with a small (< 1.5) 4000 \AA break. The stacked spectra of the 22 μ m-selected galaxies binned in IR luminosity show that the strength of the [O III] line relative to $H\beta$ grows with increasing IR luminosity. The optical spectra of the 22 μ m-selected galaxies also show that there are some ($\sim 2.8\%$) unusual galaxies with very strong [Ne III] $\lambda 3869$, 3968 emission lines that require hard ionizing radiation such as AGN or extremely young massive stars. The specific star formation rates (sSFRs) derived from the 3.6 and 22 μ m flux densities are enhanced if the 22 μ m-selected galaxies have close late-type neighbors. The sSFR distribution of the 22 μ m-selected galaxies containing active galactic nuclei (AGNs) is similar to the distribution for star-forming galaxies without AGNs. We identify 48 dust-obscured galaxy (DOG) candidates with large ($\gtrsim 1000$) mid-IR to optical flux density ratio. The combination of deep photometric and spectroscopic data with *WISE* data suggests that *WISE* can probe the universe to $z \sim 2$.

Subject headings: galaxies: active – galaxies: evolution – galaxies: formation – galaxies: starburst – infrared: galaxies – surveys

1. INTRODUCTION

The *Infrared Astronomical Satellite* (*IRAS*; Neugebauer et al. 1984) and the *AKARI* satellite (Murakami et al. 2007) conducted infrared (IR) all-sky surveys; they detected a tremendous number of IR sources over the entire sky. Recent IR satellites including *Herschel Space Observatory* (Pilbratt et al. 2010) have also carried out several small-area survey programs; they extended our understanding of the IR universe to high redshift (see Genzel & Cesarsky 2000; Soifer et al. 2008; Elbaz et al. 2011; Lutz et al. 2011; Oliver et al. 2012 for a review).

Wide-field galaxy redshift surveys (Huchra et al. 1983; de Lapparent et al. 1986; York et al. 2000; Colless et al. 2001; Jones et al. 2004; Driver et al. 2011) enlarge our view of the universe by adding the third dimension (i.e. redshift) to the projected sky (e.g., Geller & Huchra 1989; Gott et al. 2005).

The combination of “wide-field” IR and redshift surveys thus provides valuable, large samples of IR-detected galaxies without ambiguity in projection along the line of sight (e.g., Cao et al. 2006; Hwang et al. 2007; Hou et al. 2009; Wang & Rowan-Robinson 2009). These samples are an important basis for studying the optical/IR properties of IR bright galaxies and their environmental dependence (e.g., Goto 2005; Geller et al. 2006;

Hwang et al. 2010a,b; Lee et al. 2010b, 2011; Goto et al. 2011; Dariush et al. 2011; Donoso et al. 2012). There are also several redshift surveys dedicated to IR sources (see Sanders & Mirabel 1996 and Soifer et al. 2008 and references therein; see also Lake et al. 2012).

The IR bright galaxies are mainly powered by star formation (often they are also powered by active galactic nuclei (AGNs)). To understand the physical processes responsible for the IR activity, it is thus important to understand the physical parameters affecting the star formation rates (SFRs) of galaxies (see McKee & Ostriker 2007; Kennicutt & Evans 2012 for a review). The galaxy stellar mass is one of the important parameters. Empirically, the SFR per unit stellar mass (i.e. specific SFR, sSFR) is a useful indicator of SF activity (SFA) of galaxies (Brinchmann et al. 2004; Daddi et al. 2007; Pannella et al. 2009; Magdis et al. 2010; Elbaz et al. 2011).

The proximity and gas content of the nearest neighbor galaxy are also important parameters. In the hierarchical picture of galaxy formation, it is evident that galaxy interactions and mergers strongly affect the SFA of galaxies over several billion years. Observational studies clearly show that the sSFRs of IR bright galaxies are enhanced if the galaxies have gas-rich close neighbors both in low- z and in high- z universe (e.g., Geller et al. 2006; Kartaltepe et al. 2010, 2011; Hwang et al. 2010a, 2011). The presence of AGN is also an important parameter affecting the SFRs of galaxies. Recently, the interplay between AGN and SF within a galaxy is a matter of much debate: is the relationship causal or non causal? (e.g., Alexander & Hickox 2012; Mullaney et al.

¹ Smithsonian Astrophysical Observatory, 60 Garden St., Cambridge, MA 02138; hhwang@cfa.harvard.edu, mgeller@cfa.harvard.edu, mkurtz@cfa.harvard.edu, dfabricant@cfa.harvard.edu

² Department of Physics, Brown University, Box 1843, Providence, RI 02912; ian@het.brown.edu

Table 1
Number of *WISE* 22 μm Sources in the SHELS Field

22 μm Sources	$S/N_{22\mu\text{m}} \geq 5$	$S/N_{22\mu\text{m}} \geq 3$
Total	126	507
Sources with optical photometry ($R < 25.2$)	118	481
Sources with spectra ($R < 21$)	107	337
$D_n4000 \geq 1.5$	6	47
$D_n4000 < 1.5$	99	280
AGNs	58	126
DOGs	8	48
[Ne III] Strong Galaxies	5	9

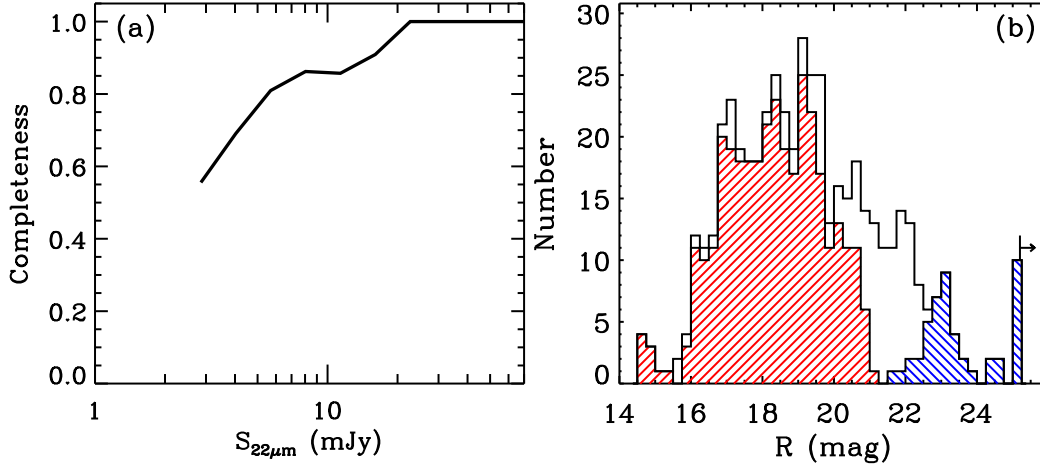


Figure 1. Spectroscopic completeness for *WISE* 22 μm sources as a function of 22 μm flux density (a). *R*-band magnitude distribution for *WISE* 22 μm sources (b). All 22 μm sources and the sources with spectroscopic redshifts are denoted by open and red hatched histograms, respectively. The dust-obscured galaxy (DOG) candidates (see Section 3.1) are indicated by a hatched histogram with orientation of 315° ($\backslash\backslash$ with blue color) relative to horizontal. The right most bin with a right arrow indicates the limiting *R*-band magnitude.

2012; Fabian 2012).

Here, we discuss the optical spectral properties of IR-selected galaxies to improve understanding of the drivers of the SFA in star-forming galaxies at intermediate redshift. We use a dense, complete redshift survey, the Smithsonian Hectospec Lensing Survey (SHELS; Geller et al. 2005, 2010, 2012), covering a 4 square degree region of a deep imaging survey, the Deep Lens Survey (DLS; Wittman et al. 2002, 2006). This region is uniformly covered by the Wide-field Infrared Survey Explorer (*WISE*; Wright et al. 2010) with excellent sensitivity in the mid-IR (MIR) bands (3.4, 4.6, 12, and 22 μm). *WISE* is 100 times more sensitive than *IRAS* at 12 μm , and has a resolution ($6''.5$ at 12 μm) much better than the arcmin resolution of *IRAS*.

Because SHELS is a magnitude-limited survey down to $R = 20.6$ (mag) without any complex selection effects, the combination of SHELS and *WISE* data provides a large, unbiased sample of *WISE*-selected galaxies with spectroscopic parameters including redshifts, 4000 \AA break and emission line fluxes.

In this study, we focus on the 22 μm -selected sample of SHELS galaxies with signal-to-noise ratio $(S/N)_{22\mu\text{m}} \geq 3$ ($\approx S_{22\mu\text{m}} > 2.5$ mJy). We discuss 12 μm -selected galaxies in a companion paper (H. S. Hwang et al. 2012, in preparation). Section 2 describes the observations. We examine the optical and MIR properties of 22 μm -selected SHELS galaxies in §3, and conclude in §4. Throughout, we adopt flat Λ CDM cosmological param-

eters: $H_0 = 70 \text{ km s}^{-1} \text{ Mpc}^{-1}$, $\Omega_\Lambda = 0.7$ and $\Omega_m = 0.3$.

2. THE DATA

2.1. SHELS

SHELS is a magnitude-limited redshift survey covering the 4 square degree region of the DLS F2 field (Geller et al. 2005, 2010, 2012). The DLS is an NOAO key program covering 20 square degrees in five separate $2^\circ \times 2^\circ$ fields (Wittman et al. 2002, 2006). The F2 field is one of the five fields and is centered on $\alpha = 09^h19^m32^s.4$ and $\delta = +30^\circ00'00''$. The DLS *R*-band images were taken in seeing $0''.9$; the source detection on these images reaches down to 28.7 mag per square arcsecond.

The spectroscopic observations for SHELS galaxies were conducted for galaxies down to $R = 20.6$ with the Hectospec 300 fiber spectrograph (Fabricant et al. 2005) on the MMT (see Geller et al. 2012 for detailed description of the spectroscopic observations). We used Hectospec's 270 line mm^{-1} grating that provides a dispersion of $1.2 \text{ \AA pixel}^{-1}$ and a resolution of $\sim 6 \text{ \AA}$. The spectra cover the wavelength range 3650 – 9150 \AA . Exposure times ranged from 0.75 to 2 hr. We also observed some galaxies fainter than $R = 20.6$ when fibers were available. The total number of objects with SHELS spectra is about 19,800 including 2874 sources with $R = 20.6 - 21$.

The spectroscopic completeness is 98% at $R \leq 20.3$, and the differential completeness for $R = 20.3 - 20.6$ is 89%. The objects missed in the spectroscopic observations at $R < 20.6$ are those near the survey edges, those

Table 2
Optical Properties of *WISE* 22 μm -selected SHELS Galaxies^a

ID	SHELS ID	R.A. ₂₀₀₀	Decl. ₂₀₀₀	R (mag)	z ^b	D_n4000	CLASS ^c
1	138.7484675+30.9888536	9:14:59.63	30:59:19.87	19.503	0.40830 ± 0.00011	1.34	U
2	138.7486030+29.7302448	9:14:59.66	29:43:48.88	12.543	0.02116 ± 0.00000	1.41	C
3	138.7555069+29.8018154	9:15:01.32	29:48:06.54	18.792	0.18112 ± 0.00006	1.48	A
4	138.7556940+29.0958824	9:15:01.37	29:05:45.18	20.335	0.33584 ± 0.00006	1.25	H
5	138.7602425+29.6844158	9:15:02.46	29:41:03.90	18.122	0.13900 ± 0.00010	1.45	C
6	138.7647624+29.2699887	9:15:03.54	29:16:11.96	13.739	0.02103 ± 0.00006	2.02	U
7	138.7815804+29.6656783	9:15:07.58	29:39:56.44	17.523	0.18445 ± 0.00010	1.71	C
8	138.7959984+30.1807242	9:15:11.04	30:10:50.61	18.945	0.09974 ± 0.00009	1.21	C
9	138.7966319+29.2524034	9:15:11.19	29:15:08.65	15.764	0.02080 ± 0.00000	1.15	H
10	138.8001139+30.0352458	9:15:12.03	30:02:06.88	16.335	0.12869 ± 0.00008	1.62	A

¹ This table is available in its entirety in a machine-readable form in the online journal. A portion is shown here for guidance regarding its form and content.

² The error of redshift is set to 0 when it is unavailable.

³ Galaxy classification (see §2.4) : H (SF), C (Composite), A (AGN from optical spectra), M (AGN from MIR colors), B (Broad-line AGN), U (Undetermined)

Table 3
WISE Properties of 22 μm -selected SHELS galaxies^a

ID	WISE ID	S _{3.4} (mJy)	S _{4.6} (mJy)	S ₁₂ (mJy)	S ₂₂ (mJy)	$\log(L_{\text{IR}}/L_{\odot})$	$\log(M_{\text{star}}/M_{\odot})$
1	J091459.67+305919.9	0.16 ± 0.01	0.10 ± 0.01	0.45 ± 0.28	2.89 ± 0.91	11.75	11.40
2	J091459.66+294349.0	27.36 ± 0.55	17.87 ± 0.33	104.99 ± 1.35	167.80 ± 3.25	10.64	11.08
3	J091501.32+294806.4	0.20 ± 0.01	0.29 ± 0.02	1.10 ± 0.13	4.59 ± 0.98	11.08	10.64
4	J091501.41+290545.5	0.03 ± 0.01	0.07 ± 0.01	0.46 ± 0.13	3.50 ± 0.93	11.62	10.35
5	J091502.47+294103.8	0.53 ± 0.02	0.42 ± 0.02	2.38 ± 0.15	6.99 ± 0.99	10.99	10.89
6	J091503.55+291612.1	5.62 ± 0.11	2.74 ± 0.06	1.67 ± 0.14	3.07 ± 0.95	9.11	10.29
7	J091507.60+293956.1	0.91 ± 0.02	0.70 ± 0.02	1.30 ± 0.14	3.96 ± 0.97	11.04	11.42
8	J091511.05+301050.5	0.06 ± 0.01	0.04 ± 0.01	0.31 ± 0.77	2.92 ± 0.86	10.36	9.60
9	J091511.17+291508.1	1.38 ± 0.05	0.94 ± 0.04	5.24 ± 0.25	6.84 ± 1.68	9.42	9.58
10	J091512.03+300207.0	1.17 ± 0.03	0.82 ± 0.03	2.56 ± 0.14	3.38 ± 0.88	10.64	11.30

¹ This table is available in its entirety in a machine-readable form in the online journal. A portion is shown here for guidance regarding its form and content.

near bright stars, or point sources.

2.2. *WISE*

We use the *WISE* all-sky survey catalog³, containing uniform photometric data for over 563 million objects at 4 MIR bands (3.4, 4.6, 12 and 22 μm). *WISE* covers the entire region of the SHELS field to a homogeneous depth. We use the point source profile-fitting magnitudes, and restrict our analysis to the sources with $S/N \geq 3$ at 22 μm . The *WISE* 5σ photometric sensitivity is estimated to be better than 0.08, 0.11, 1 and 6 mJy at 3.4, 4.6, 12 and 22 μm in unconfused regions on the ecliptic plane (Wright et al. 2010).

After rejecting bright stars through visual inspection of their optical images, we have 507 sources with 22 μm detection ($S/N \geq 3$) in the SHELS field. We cross-correlate these IR sources with the objects in the DLS *R*-band source catalog (down to $R < 25.2$) with a matching tolerance of $3''$ ($\sim 0.5 \times \text{FWHM}$ of the *WISE* PSF at 3.4 μm). We identify 481 matches and 26 sources without optical counterparts. Among the 481 matches, there are 337 (107) galaxies with $S/N_{22\mu\text{m}} \geq 3$ (≥ 5) and a measured redshift in SHELS. We discuss the sources without optical counterparts in Section 3.1.

Table 1 summarizes the statistics for the number of

WISE 22 μm sources in our sample. Figure 1 shows the spectroscopic completeness for *WISE* 22 μm sources (left panel). The completeness is 100% at $\gtrsim 20$ mJy, and reaches $\sim 60\%$ even at the faintest level of ~ 3 mJy. We also show the *R*-band magnitude distribution of the 22 μm sources in the right panel. As expected, most 22 μm sources at $R < 20.6$ have spectroscopic redshifts (red hatched histogram).

We list 337 galaxies with $S/N_{22\mu\text{m}} \geq 3$ and spectroscopic redshifts in Table 2 with their optical properties including *R*-band magnitude, redshift, D_n4000 , and SF/AGN classification. We also list the *WISE* properties of these galaxies including the IR luminosity derived from the 22 μm flux density and the stellar mass from the 3.4 μm flux density (see Section 2.3) in Table 3.

We show the spatial distribution of the 22 μm -selected SHELS galaxies (red circles) in company with all SHELS galaxies regardless of *WISE* detection (gray dots) in Figure 2. Some galaxy clusters are obvious in the distribution of all SHELS galaxies on the sky (see Geller et al. 2010 for a list of candidate clusters), but the 22 μm -selected galaxies are less strongly clustered. These 22 μm -selected galaxies are mainly star-forming galaxies; thus they tend to avoid the core region of clusters as expected (e.g., Park & Hwang 2009).

Figure 3 shows the redshift distribution of all SHELS galaxies (a) and of *WISE* 22 μm -selected galaxies (b).

³ <http://wise2.ipac.caltech.edu/docs/release/allsky/expsup/>

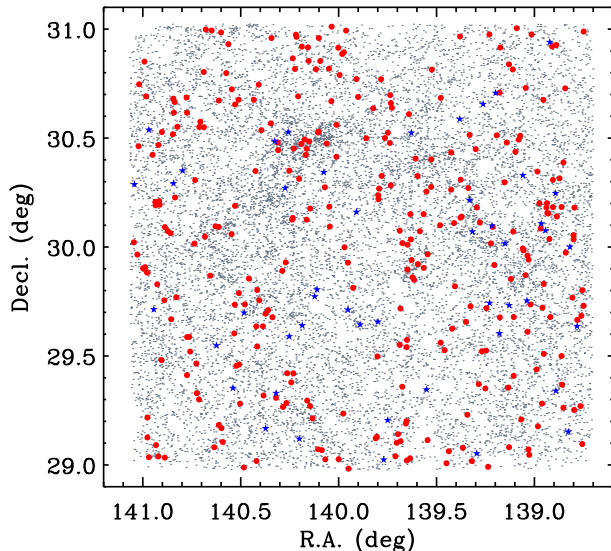


Figure 2. Spatial distribution of SHELs galaxies on the sky. The red circles are *WISE* 22 μm -selected galaxies, and gray dots are all SHELs galaxies regardless of *WISE* detection. Blue star symbols are DOG candidates (see Section 3.1).

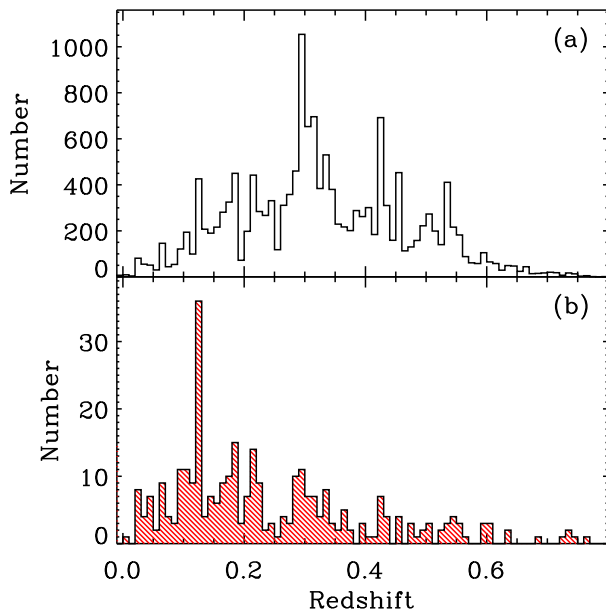


Figure 3. Redshift distribution of all SHELs galaxies (a) and of 22 μm -selected galaxies (b).

The redshift distribution of all SHELs galaxies in panel (a) shows dominant peaks around $z \sim 0.3$ and 0.4 , indicating the presence of galaxy clusters (Geller et al. 2010). Interestingly, there is a prominent peak for 22 μm -selected galaxies in panel (b) at $z \sim 0.13$. This peak corresponds to a galaxy group (see Geller et al. 2010). However, the 22 μm -selected galaxies are not centrally concentrated, but are in the outskirts of the group.

Figure 4 shows a cone diagram projected along the declination direction. We project the entire right ascension range onto the declination-redshift plane. The red circles are 22 μm -selected galaxies, and the gray dots are all SHELs galaxies regardless of *WISE* detection. There are detections up to $z \sim 0.77$ (there are also 20 galaxies/quasars at $z = 0.8 - 3.0$ not shown in the figure).

The figure shows again that the 22 μm -selected galaxies avoid the highest density regions as expected.

2.3. Stellar Masses and SFRs of *WISE* 22 μm -selected Galaxies

WISE 3.4 μm data probe the old stellar components dominating the stellar mass of galaxies. Thus the rest-frame luminosity around this wavelength can be a useful tracer of stellar mass (e.g., Hancock et al. 2007; Ko et al. 2012; Lin et al. 2012). There are other components contributing at this wavelength including 3.3 μm polycyclic aromatic hydrocarbon (PAH) emission and AGN dust emission (Lu et al. 2003; Flagey et al. 2006; Magnelli et al. 2008; Lee et al. 2012), but they seem to have little effect on the correlation between stellar mass and 3.4 μm rest-frame luminosity (see also Draine et al. 2007). To determine the correlation between stellar mass and 3.4 μm rest-frame luminosity, we plot stellar masses derived from the SDSS data against 3.4 μm rest-frame luminosities for SHELs galaxies in Figure 5. We use stellar mass estimates for the spectroscopic sample of SDSS galaxies from the MPA/JHU DR7 value-added galaxy catalog⁴ (VAGC). These estimates are based on the fit of SDSS five-band photometry to the models of Bruzual & Charlot (2003) (see also Kauffmann et al. 2003a). We convert the stellar masses in the MPA/JHU DR7 VAGC that are based on the Kroupa IMF (Kroupa 2001) to those with Salpeter IMF (Salpeter 1955) by dividing them by a factor of 0.7 (Elbaz et al. 2007).

To compute the rest-frame luminosity in the *WISE* bands, we use the fitting code and the templates in Assef et al. (2010). The code utilizes a set of low-resolution empirical spectral energy distribution (SED) templates covering the wavelengths 0.03 – 30 μm . The templates include an old stellar population, a continuously star-forming population, a starburst population, and AGNs with varying amounts of reddening and absorption by the intergalactic medium. We apply this code to our combined data set of SDSS *ugriz*, KPNO *R*, *WISE* 3.4, 4.6, 12 and 22 μm photometry. To remove the AGN contribution from the 3.4 μm luminosity, we estimate the AGN contribution to the 3.4 μm luminosity based on the Assef et al. templates. The median AGN contribution to the 3.4 μm luminosity for the 22 μm -selected galaxies is only 6%. For each galaxy, we subtract the AGN contribution from the 3.4 μm luminosity and use this quantity to derive a correlation with SDSS mass estimate.

Figure 5 demonstrates the tight correlation between 3.4 μm rest-frame luminosities and stellar masses derived from the SDSS data, suggesting that 3.4 μm rest-frame luminosity is indeed a good tracer of stellar mass (once AGN contribution is removed). We use the bisector method (Isobe et al. 1990) to fit the correlation, and obtain the relation,

$$\log(M_{\text{star}}/M_{\odot}) = \log(\nu L_{\nu}(3.4\mu\text{m})/L_{\odot}) \times (1.14 \pm 0.02) - (0.11 \pm 0.17). \quad (1)$$

We use this equation to compute stellar masses for all of the SHELs 22 μm -selected galaxies except the broad-line AGNs where the AGN component dominates the SED.

We compute the IR luminosities (L_{IR}) for 22 μm -selected galaxies from their 22 μm flux densities because

⁴ <http://www.mpa-garching.mpg.de/SDSS/DR7/Data/stellarmass.html>

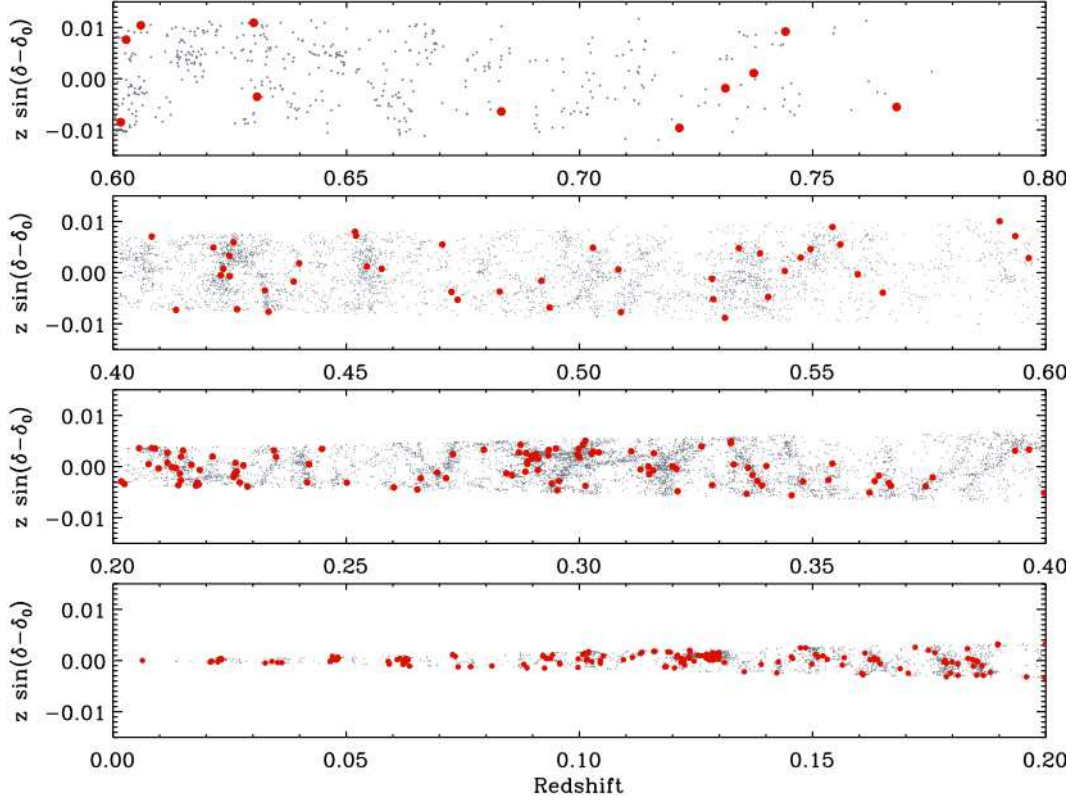


Figure 4. Redshift cone diagram for SHELS galaxies projected along the declination direction. We project the entire right ascension range onto the declination-redshift plane. The red circles are *WISE* 22 μm -selected galaxies, and gray dots are all SHELS galaxies regardless of *WISE* detection.

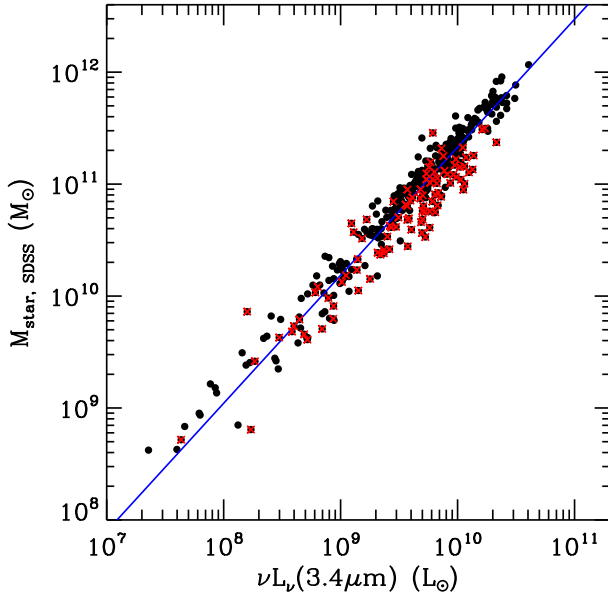


Figure 5. Stellar mass from the SDSS database vs. rest-frame 3.4 μm luminosity for SHELS galaxies regardless of 22 μm detection (black circles). The AGN contribution to the 3.4 μm luminosity is removed with the SED fit. The solid line is the best fit with an ordinary least-squares bisector method (see equation (1)). Red crosses are 22 μm -selected galaxies.

22 μm data are closer to the peak of IR emission than the other *WISE* bands and because they are less affected by PAH emission features. We use the SED templates of Chary & Elbaz (2001) as a basis for the SED fit. IR luminosities extrapolated from a single passband have

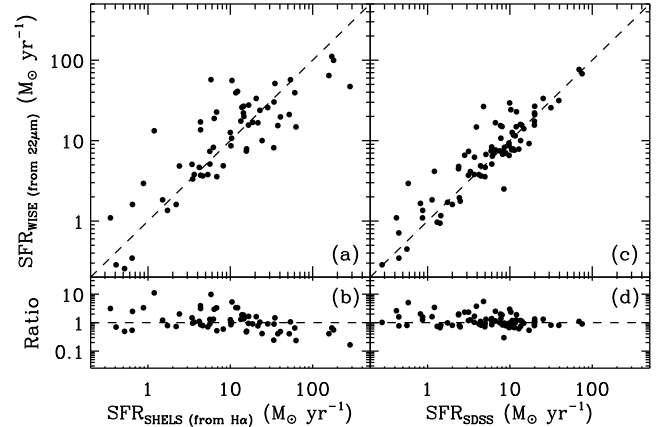


Figure 6. Comparison of SFRs from *WISE* 22 μm flux density (SFR_{WISE}) with those from SHELS MMT spectra ($\text{SFR}_{\text{SHELS}}$, a-b) and from SDSS spectra (SFR_{SDSS} , c-d). We plot only galaxies with $\text{S/N}_{\text{H}\alpha} \geq 20$. The dashed line in each panel indicates the one-to-one relation.

been examined in many papers; they agree very well with those measured with all FIR bands even in the presence of AGNs (Elbaz et al. 2010, 2011). They also agree with the optical spectra (Hwang et al. 2012a). However, it should be noted that the SFRs converted from IR luminosities for AGN-host galaxies (see Section 3.3) indicate a upper limit on the SFRs of their host galaxies. An SED analysis with data points at $\lambda > 22 \mu\text{m}$ is necessary to estimate the AGN contribution at 22 μm correctly.

As a consistency check, we compare SFRs converted from IR luminosities (SFR_{WISE}) with those from MMT and SDSS optical spectra ($\text{SFR}_{\text{SHELS}}$ and SFR_{SDSS}) in

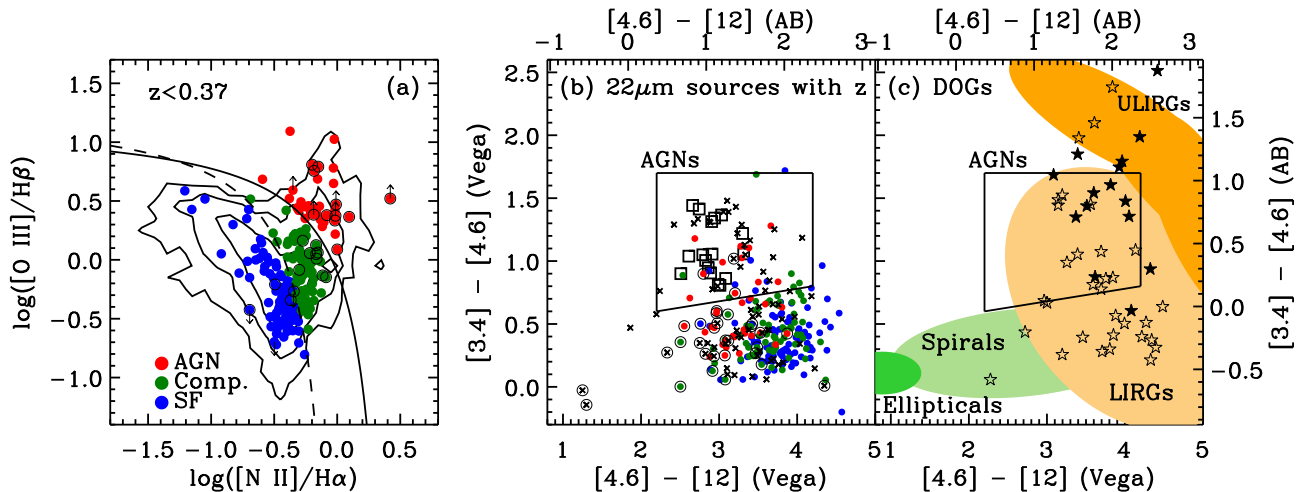


Figure 7. AGN diagnostic diagrams for galaxies based on optical $[\text{O III}]/\text{H}\beta$ vs. $[\text{N II}]/\text{H}\alpha$ line ratios (a) and on *WISE* colors (b-c). The solid and dashed lines in (a) indicate the extreme starbursts (Kewley et al. 2001) and pure SF limits (Kauffmann et al. 2003b), respectively. The contours indicate the distribution of all SHELs galaxies regardless of *WISE* detection. The lowest contour level encloses 95% of SHELs galaxies. Different colored symbols represent different classes (AGN: red, Composite: green, SF: blue). Galaxies with $S/N < 3$ for $\text{H}\beta$ and for $[\text{O III}]$ are shown as up and down arrows, respectively. Galaxies with $D_n4000 \geq 1.5$ are represented by black open circles. We plot only galaxies at $z < 0.37$. In (b), we plot all $22\text{ }\mu\text{m}$ -selected SHELs galaxies with spectroscopic redshifts. Crosses in (b) are galaxies not classified in panel (a). Open squares are broad-line AGNs, and open circles are galaxies with $D_n4000 \geq 1.5$. Panel (c) shows *WISE* colors for DOG candidates (filled star: $S/N \geq 3$ at all bands, open star: $S/N < 3$ at least one band). Solid lines in (b-c) are the MIR AGN selection criteria proposed by Jarrett et al. (2011), respectively. We mark several regions occupied by interesting classes of objects (ellipticals, spirals, LIRGs and ULIRGs; see Figure 12 in Wright et al. 2010).

Figure 6. We convert the IR luminosity into SFR_{WISE} using the relation in Kennicutt (1998) with the assumption of a Salpeter IMF: $\text{SFR}_{\text{WISE}} (M_{\odot} \text{ yr}^{-1}) = 1.72 \times 10^{-10} L_{\text{IR}} (L_{\odot})$. We adopt $\text{SFR}_{\text{SHELs}}$ from Westra et al. (2010), who compute the aperture and extinction-corrected SFRs from the $\text{H}\alpha$ fluxes derived from the MMT spectra. A typical aperture correction factor defined by $A = 10^{-0.4(m_{\text{total}} - m_{\text{fiber}})}$ for $22\text{ }\mu\text{m}$ -selected galaxies is 4.8 where m_{total} and m_{fiber} are total and fiber R -band magnitudes, respectively (see Fig. 2 in Westra et al. 2010). A typical V -band extinction A_V with Calzetti et al. (2000) reddening law for $22\text{ }\mu\text{m}$ -selected galaxies is 2.0 (see Fig. 3 in Westra et al. 2010), consistent with the values for similar MIR-selected galaxies (e.g., see Fig. 11 in Caputi et al. 2008). The SFR_{SDSS} is from the MPA/JHU DR7 VAGC (Brinchmann et al. 2004), which provides the extinction and aperture corrected SFRs. We convert the SFR_{SDSS} in MPA/JHU DR7 VAGC based on the Kroupa IMF to the Salpeter IMF by dividing the SFR_{SDSS} by a factor of 0.7.

The comparison of SFR_{WISE} with $\text{SFR}_{\text{SHELs}}$ and SFR_{SDSS} shows that SFR_{WISE} agrees well overall with the measurements from the optical spectra, demonstrating the consistency between the two measurements. Scatter in the correlation results from uncertain aperture and reddening corrections. The SHELs galaxies in the left panel ($\langle z \rangle \sim 0.14$) are on average more distant than the SDSS galaxies in the right panel ($\langle z \rangle \sim 0.1$). The fiber diameter for SHELs spectra ($1''.5$) is smaller than that for SDSS spectra ($3''$). The scatter is thus slightly larger for SHELs galaxies.

2.4. AGN Selection

To identify AGN host galaxies among *WISE* $22\text{ }\mu\text{m}$ -selected galaxies, we use the Baldwin-Phillips-Terlevich (BPT) line ratio diagram based on $[\text{O III}]/\text{H}\beta$ and $[\text{N II}]/\text{H}\alpha$ (Baldwin et al. 1981; Veilleux & Osterbrock

1987). We apply this method only to galaxies at $z < 0.37$ because the $\text{H}\alpha$ line for galaxies at $z > 0.37$ is redward of the Hectospec spectral coverage ($3650 - 9150\text{ }\text{\AA}$). We adopt line flux measurements from Westra et al. (2010), who provide the emission-line fluxes from the continuum subtracted spectra of SHELs galaxies based on stellar population synthesis models of Bruzual & Charlot (2003).

We plot the line ratios of *WISE* $22\text{ }\mu\text{m}$ -selected galaxies in Figure 7(a) along with all SHELs galaxies (contours). For galaxies with $S/N \geq 3$ in all four lines, we classify them (star-forming galaxies, AGNs, and composite galaxies) based on their relative positions with respect to the demarcation lines identifying extreme starbursts (Kewley et al. 2001) and pure SF (Kauffmann et al. 2003b). If the S/N of $\text{H}\beta$ or $\text{H}\alpha$ is < 3 (but S/N s of $[\text{O III}]$ and $[\text{N II}]$ are ≥ 3), we adopt the 3σ upper limit values as line fluxes following Westra et al. (2010). We use these upper limits to compute the line ratios, and classify them only if they fall in the regions occupied by composite galaxies and AGNs. There are five galaxies with very low S/N in $\text{H}\beta$; we show them in panel (a) with up arrows. Similarly, if the S/N of $[\text{O III}]$ or $[\text{N II}]$ is < 3 (but S/N s of $\text{H}\beta$ and $\text{H}\alpha$ are ≥ 3), we classify them only if they fall in the region occupied by SF galaxies by adopting the 3σ upper limits as line fluxes. There are three galaxies with very low S/N in $[\text{O III}]$ (down arrows).

We identify 17 broad emission-line AGNs. The FWHM of the broad component of the Balmer or $\text{Mg II } \lambda 2800$ lines exceeds 2000 km s^{-1} . The amplitude of the broad component exceeds the local rms of the continuum-subtracted spectra.

To identify additional AGNs missed by the spectral diagnostics, we use the *WISE* color-color diagram in panel (b). We adopt the AGN selection criteria proposed by Jarrett et al. (2011) (solid lines in b). There are 64 AGNs

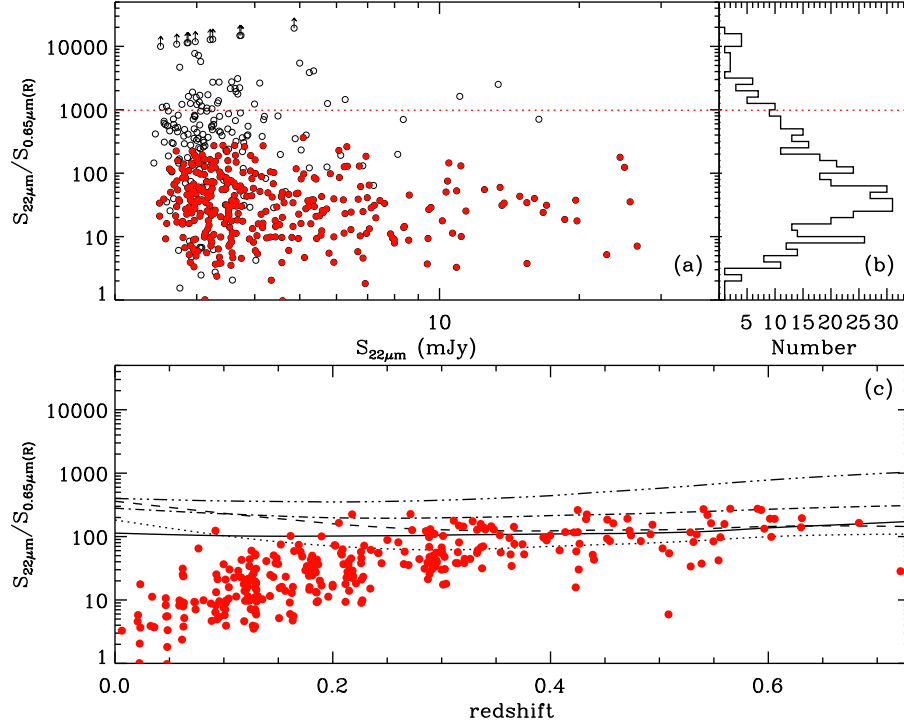


Figure 8. The flux density ratio between *WISE* 22 μ m and *R*-band as a function of 22 μ m flux density (a), and its histogram (b). Filled red (open black) circles are galaxies with (without) spectroscopic redshifts. Galaxies with arrows have only an upper limit *R*-band flux density. The flux density ratio as a function of redshift (c). We overplot the expected ratios from several SED templates of local star-forming, or AGN-host galaxies (Polletta et al. 2007, M82: solid, Arp220: dotted, IRAS 22491-1808: dashed, Mrk 231: dash dot, IRAS 19254-7245 South: dash dot dot dot).

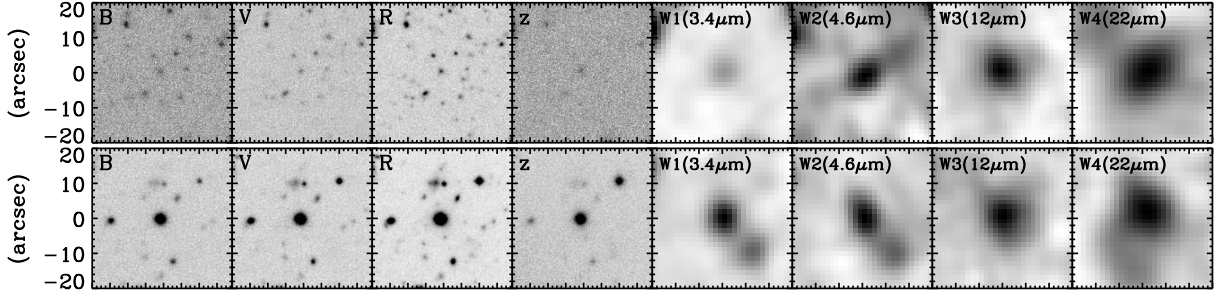


Figure 9. *BVRz* and *WISE* 3.4, 4.6, 12 and 22 μ m cutout images ($40'' \times 40''$) for a DOG candidate (*WISE* ID: J092129.47+291003.1, $S_{22\mu\text{m}} = 5.00 \pm 0.93$ mJy, and $R=23.8$ mag) (Top) and for a typical 22 μ m-selected galaxy (*WISE* ID: J092221.93+290619.8, $S_{22\mu\text{m}} = 5.00 \pm 0.97$ mJy, and $R=19.2$ mag) (Bottom).

satisfying these *WISE* color criteria ($\sim 23\%$ among the galaxies in this panel). Among them, 34 and 5 galaxies are classified as AGN and SF based on their optical spectra, respectively; the five SF galaxies may contain obscured AGNs (e.g., Veilleux et al. 2009; Lee et al. 2012). The remaining 25 galaxies cannot be classified with their optical spectra. We replace the galaxy classification with the one based on *WISE* colors only if their classifications based on the optical spectra are either SF or undetermined (see Table 2).

In summary, among 259 *WISE* 22 μ m-selected galaxies at $z < 0.37$, 219 galaxies are classified based on the optical line ratio diagram (a): 17%, 36% and 47% as AGN, composite and SF galaxies, respectively. If we include AGNs identified by the *WISE* color-color diagram and by broad emission lines, the AGN fraction remains similar: 19%. For the analysis below, we include composite galaxies in the sample of AGNs. Among 78 galaxies at

$z \geq 0.37$, we have 36 AGNs ($\sim 46\%$) including 25 from the *WISE* color-color diagram and 11 broad-line AGNs identified from the spectroscopy.

3. RESULTS AND DISCUSSION

3.1. Dust-Obscured Galaxies (DOGs)

Among the 481 22 μ m sources with optical counterparts in the DLS *R*-band catalog, 144 sources do not have spectroscopic redshifts (see Section 2.2). We examined optical images of these 144 sources. The majority of these objects are indeed fainter than the magnitude limit of SHELS (i.e. $R > 20.6$, see Figure 1(b)). The sources at $R < 20.6$ missed by SHELS spectroscopy are mainly point sources or galaxies close to bright stars.

The optically faint 22 μ m-selected galaxies probably result from large dust obscuration. To study their properties in detail, we plot the *WISE* 22 μ m to *R*-band flux density ratio as a function of 22 μ m flux density in the

Table 4
Dust-obscured galaxies in the SHELS field

ID	WISE ID	R ^a (mag)	S _{3.4} ^b (mJy)	S _{4.6} (mJy)	S ₁₂ (mJy)	S ₂₂ (mJy)	Comment
1	J091507.75+293811.9	23.064	0.06 ± 0.01	0.17 ± 0.02	1.16 ± 0.14	3.05 ± 0.94	Near edge of field
2	J091516.57+300001.0	99.999	0.04 ± 0.01	0.03 ± 0.01	0.23 ± 0.00	2.51 ± 0.85	
3	J091518.50+290907.5	23.039	0.06 ± 0.01	0.15 ± 0.01	0.48 ± 0.12	3.17 ± 0.88	Two sources separated by 2''.5
4	J091533.73+292025.2	22.790	0.04 ± 0.01	0.04 ± 0.00	0.26 ± 0.00	2.91 ± 0.82	Offset 0''.4 from <i>WISE</i> position
5	J091534.16+301448.1	99.999	0.03 ± 0.01	0.03 ± 0.00	0.23 ± 0.00	2.87 ± 0.82	
6	J091541.22+305624.7	23.015	0.04 ± 0.01	0.06 ± 0.00	0.46 ± 0.14	3.64 ± 0.92	Offset 1''.3 from <i>WISE</i> position
7	J091546.49+300432.8	23.079	0.01 ± 0.01	0.07 ± 0.01	0.47 ± 0.00	2.88 ± 0.95	Offset 0''.5 from <i>WISE</i> position
8	J091551.66+300627.8	24.386	0.04 ± 0.01	0.05 ± 0.01	0.25 ± 0.00	3.06 ± 0.88	
9	J091609.21+294513.9	22.632	0.05 ± 0.01	0.07 ± 0.01	0.25 ± 0.00	3.07 ± 0.87	
10	J091614.15+301944.8	22.421	0.04 ± 0.01	0.03 ± 0.01	0.32 ± 0.14	4.00 ± 1.09	
11	J091630.98+294357.5	22.112	0.09 ± 0.01	0.30 ± 0.02	2.62 ± 0.15	6.26 ± 1.14	Point Source
12	J091636.07+300058.5	24.276	0.04 ± 0.01	0.07 ± 0.01	0.24 ± 0.00	2.76 ± 0.90	
13	J091642.83+293613.1	22.049	0.26 ± 0.01	0.51 ± 0.02	2.10 ± 0.14	5.74 ± 0.99	
14	J091647.60+304225.0	22.662	0.08 ± 0.01	0.06 ± 0.01	0.27 ± 0.00	3.33 ± 0.96	
15	J091652.05+300553.0	22.997	0.05 ± 0.01	0.10 ± 0.02	0.34 ± 0.13	2.99 ± 0.93	
16	J091654.90+294434.4	22.716	0.06 ± 0.01	0.05 ± 0.01	0.30 ± 0.00	3.00 ± 0.91	
17	J091702.90+303921.0	99.999	0.05 ± 0.01	0.08 ± 0.01	0.42 ± 0.00	2.98 ± 0.97	Between three faint sources
18	J091710.73+290309.8	22.465	0.07 ± 0.01	0.08 ± 0.01	0.42 ± 0.00	3.24 ± 0.91	Offset 0''.5 from <i>WISE</i> position
19	J091716.01+300413.9	24.642	0.04 ± 0.01	0.04 ± 0.00	0.50 ± 0.13	3.03 ± 0.93	close pair with galaxy 2'' away
20	J091719.57+301253.9	99.999	0.06 ± 0.01	0.05 ± 0.00	0.50 ± 0.00	3.25 ± 1.05	
21	J091731.51+303514.6	21.886	0.09 ± 0.01	0.48 ± 0.02	5.21 ± 0.18	13.38 ± 1.07	
22	J091812.20+292045.6	99.999	0.01 ± 0.00	0.05 ± 0.00	0.26 ± 0.00	4.86 ± 0.94	
23	J091830.86+303127.7	99.999	0.43 ± 0.01	0.25 ± 0.02	0.37 ± 0.00	2.86 ± 0.91	
24	J091859.82+291218.8	23.516	0.05 ± 0.01	0.10 ± 0.01	0.47 ± 0.00	3.67 ± 0.97	
25	J091904.71+290125.6	22.807	0.07 ± 0.01	0.07 ± 0.02	0.43 ± 0.00	2.58 ± 0.86	Companion galaxy 3'' away
26	J091911.74+293925.8	22.906	0.05 ± 0.01	0.11 ± 0.02	0.49 ± 0.14	3.68 ± 0.96	Three sources within 5'' of <i>WISE</i> position
27	J091933.61+293838.7	23.143	0.13 ± 0.01	0.31 ± 0.02	1.56 ± 0.14	3.63 ± 1.01	
28	J091938.12+300938.4	23.221	0.09 ± 0.01	0.19 ± 0.02	1.39 ± 0.13	4.10 ± 1.00	Multiple sources within 3''
29	J091948.45+294242.9	23.226	0.06 ± 0.01	0.09 ± 0.01	0.39 ± 0.13	2.94 ± 0.98	Offset 1''.5 from <i>WISE</i> position
30	J092018.07+302034.7	23.162	0.04 ± 0.01	0.05 ± 0.01	0.34 ± 0.00	3.54 ± 0.96	Offset 1''.2 from <i>WISE</i> position
31	J092026.39+294817.4	23.508	0.06 ± 0.01	0.04 ± 0.02	0.27 ± 0.00	3.25 ± 1.02	
32	J092029.31+294622.8	22.521	0.06 ± 0.01	0.04 ± 0.02	0.37 ± 0.00	3.15 ± 0.99	
33	J092044.55+293824.4	22.749	0.12 ± 0.01	0.09 ± 0.01	0.30 ± 0.13	3.34 ± 0.87	Five sources within 5''
34	J092048.18+290710.7	21.620	0.16 ± 0.01	0.21 ± 0.02	2.11 ± 0.14	11.06 ± 1.07	Offset 1'' from <i>WISE</i> position
35	J092100.52+293523.0	99.999	0.08 ± 0.01	0.09 ± 0.01	0.24 ± 0.00	2.72 ± 0.89	
36	J092101.74+303140.5	99.999	0.12 ± 0.01	0.09 ± 0.01	0.50 ± 0.00	3.74 ± 0.98	
37	J092105.59+301614.7	23.368	0.11 ± 0.01	0.20 ± 0.02	1.57 ± 0.13	5.24 ± 0.92	
38	J092116.64+291946.2	24.740	0.02 ± 0.01	0.08 ± 0.01	0.35 ± 0.14	2.97 ± 0.96	Four sources within 4''
39	J092118.29+302910.2	23.477	0.13 ± 0.01	0.17 ± 0.02	0.85 ± 0.13	3.35 ± 0.96	
40	J092129.47+291003.1	23.793	0.04 ± 0.01	0.09 ± 0.01	1.79 ± 0.13	5.00 ± 0.93	
41	J092155.82+294154.5	22.798	0.09 ± 0.01	0.09 ± 0.02	0.28 ± 0.00	3.04 ± 0.95	Other source 2''.5 away
42	J092209.52+292110.0	22.793	0.04 ± 0.01	0.03 ± 0.01	0.34 ± 0.12	2.53 ± 0.83	
43	J092229.73+293254.0	23.145	0.11 ± 0.01	0.26 ± 0.02	1.63 ± 0.14	3.71 ± 0.96	
44	J092311.14+302101.8	22.801	0.13 ± 0.01	0.12 ± 0.02	0.96 ± 0.13	2.79 ± 0.91	Three overlapping sources
45	J092322.42+301730.9	23.412	0.15 ± 0.01	0.45 ± 0.02	1.91 ± 0.14	5.36 ± 1.01	
46	J092346.50+294250.0	23.420	0.07 ± 0.01	0.21 ± 0.02	1.49 ± 0.13	3.57 ± 0.87	
47	J092352.59+303215.9	99.999	0.05 ± 0.01	0.12 ± 0.01	0.42 ± 0.00	3.72 ± 0.91	
48	J092410.27+301716.8	99.999	0.17 ± 0.01	0.14 ± 0.02	0.32 ± 0.00	3.21 ± 0.94	

¹ When there is no optical counterpart, the *R*-band magnitude is set to 99.999.

² When the flux density error is equal to 0, the flux density indicates the upper limit.

upper panel of Figure 8. We indicate the objects without optical counterparts with arrows based on the upper limit of the available *R*-band magnitudes (i.e. $R \sim 25.2$).

Galaxies with very large $S_{24\mu\text{m}}/S_{0.65\mu\text{m}(R)}$ are known as dust-obscured galaxies (DOGs, Dey et al. 2008). Dey et al. (2008) used *Spitzer* 24 μm flux density to define DOGs as objects with $S_{24\mu\text{m}}/S_{0.65\mu\text{m}} \geq 982$ or $(R - [24]) \geq 14$ (Vega) mag. They use various spectroscopic observations (primarily IR spectroscopy) to show that most of these objects are $z \sim 2$ galaxies with large ratios between rest-frame MIR and UV flux densities. These large ratios seem to result from abnormally large dust obscuration in the UV rather than from enormously large MIR emission (e.g., Penner et al. 2012).

We use the Dey et al. criterion (i.e. $S_{22\mu\text{m}}/S_{0.65\mu\text{m}} \geq 982$) to select DOGs among the 22 μm -selected SHELS

galaxies (dotted line in the upper panel of Figure 8). Because of the difference in bandpasses between *Spitzer* 24 μm and *WISE* 22 μm , the *WISE* 22 μm flux density for DOG selection criterion could be smaller by $\sim 10\%$ (i.e. $S_{22\mu\text{m}}/S_{0.65\mu\text{m}} \lesssim 0.9 \times 982$) if we assume the spectrum of M82 or Arp220 at $z \sim 2$. However, we retain the $S_{22\mu\text{m}}/S_{0.65\mu\text{m}} \geq 982$ for our selection criterion of DOGs.

We identify 48 DOG candidates in the SHELS field. Their *WISE* colors suggest that 50% of these objects contain AGNs (see Figure 7(c)); the rest of them are LIRGs or ULIRGs. We list the DOG candidates in Table 4 with their *R*-band magnitudes and *WISE* flux densities at each wavelength. Figure 2 shows their spatial distribution on the sky. We show an example of optical *BVRz* and *WISE* 3.4, 4.6, 12 and 22 μm cutout images

for a DOG candidate in the top panel of Figure 9. We also show a typical 22 μm -selected galaxy with similar 22 μm flux density in the bottom panel for comparison. The optical counterpart for the DOG is barely visible even in the very deep DLS images.

To study the redshift dependence of the flux density ratio between *WISE* 22 μm and *R*-band, we plot $S_{22\mu\text{m}}/S_{0.65\mu\text{m}}$ of galaxies as a function of redshift (lower panel in Figure 8). We overplot the flux density ratios expected from several SED templates of local star-forming, or AGN-host galaxies (Polletta et al. 2007, M82: solid, Arp220: dotted, IRAS 22491-1808: dashed, Mrk 231: dash dot, IRAS 19254-7245 South: dash dot dot dot). Interestingly, all the observational data points with large flux density ratios are covered by the local SED templates. None of templates have flux density ratios larger than ~ 1000 , which would satisfy the DOG criterion in this redshift range. If we compute the flux density ratios of these SED templates at $z \sim 2$, none of these templates except IRAS 19254-7245 South⁵ satisfy the DOG criterion (see also Figure 1 in Dey et al. 2008).

3.2. Spectral Properties of 22 μm -selected Galaxies

In this section, we compare the spectral parameters of the 22 μm -selected galaxies with those of other SHELS galaxies. We then discuss the properties of average spectra of the 22 μm -selected galaxies. We also show some unusual galaxies with [Ne III] strong emission.

3.2.1. Spectral Parameters

In Figure 10, we plot several physical parameters of the 22 μm -selected galaxies as a function of redshift. In the top panel (a), we show the distribution of D_n4000 (a measure of the 4000 \AA break). This measure was originally defined by Bruzual (1983) as $D4000$, the ratio of the average flux density F_ν in the band 4050 – 4250 \AA to the band 3750 – 3950 \AA . This definition was revised by Balogh et al. (1999) as D_n4000 using the narrower continuum bands (4000 – 4100 and 3850 – 3950 \AA). The Balogh et al. definition is less sensitive to reddening. This 4000 \AA break results from an accumulation of absorption lines of ionized metals in low mass stars at wavelength $< 4000 \text{\AA}$. The amplitude of the break is smaller in galaxies with young stellar populations because the opacity decreases in hot young stars. It is larger for old metal-rich populations. Therefore, D_n4000 is a useful measure of the age of the stellar population.

We adopt the D_n4000 measurements for SHELS galaxies from Woods et al. (2010). The internal systematic error in our D_n4000 values based on repeated measurements is only 4.5%. Our D_n4000 measurements from MMT and SDSS spectra for the galaxies in common between SHELS and SDSS agree very well with a median ratio of 1.00 (Fabricant et al. 2008). The panel (a) shows that the D_n4000 distribution for all SHELS galaxies is bimodal, underscoring the existence of two well-known galaxy populations: one dominated by old stars and the other with recent star formation. Following Kauffmann et al. (2003a), we divide the two

⁵ IRAS 19254-7245 South satisfies the DOG criterion at $z \sim 2$, but the relevant UV SED of this galaxy is not well constrained (see Berta et al. 2003).

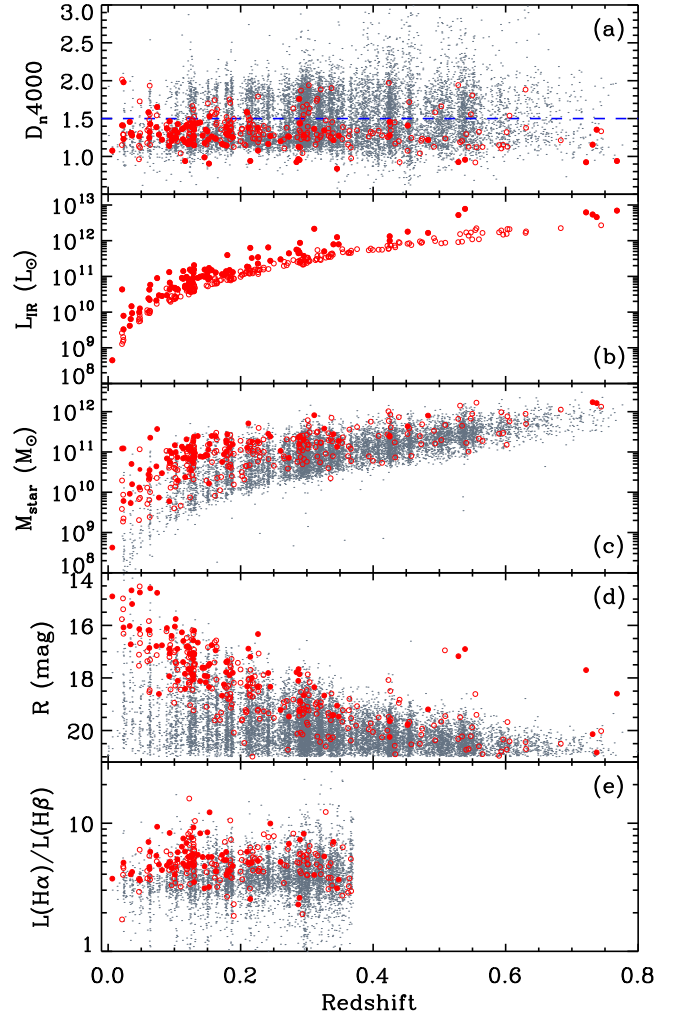


Figure 10. D_n4000 (a), IR luminosity (b), stellar mass (c), *R*-band magnitude (d), and $H\alpha/H\beta$ (e) as a function of redshift. Gray dots indicate all SHELS galaxies. Red filled and open circles indicate 22 μm -selected galaxies with $(S/N)_{22\mu\text{m}} \geq 5$ and ≥ 3 , respectively. Horizontal dashed lines in (a) indicate $D_n4000 = 1.5$ that divides galaxies into subsets dominated by old and young stellar populations. Red circles with $z > 0.5$ and $R \approx 17 - 18.5$ are quasars from the SDSS.

populations at $D_n4000 = 1.5$ (blue, dashed horizontal lines). Kauffmann et al. (2003a) showed that galaxies with $D_n4000 < 1.5$ contain young stellar populations with $\lesssim 1$ Gyr.

If 22 μm -selected galaxies are powered by recent SF or nuclear activity, their stellar populations should be young (i.e. small D_n4000). As expected, most 22 μm -selected galaxies have small D_n4000 ($\sim 86\%$; 60% of all SHELS galaxies have $D_n4000 < 1.5$), but there are some 22 μm -selected galaxies with large D_n4000 (see Section 3.3). We use the Kolmogorov-Smirnov (K-S) test to determine whether the D_n4000 distributions of 22 μm -selected and all SHELS galaxies are drawn from the same distribution. To have a fair comparison, we construct 1000 trial data sets by randomly selecting galaxies among all SHELS galaxies to have the same number of galaxies and to have the same redshift distribution as the 22 μm -selected galaxies. We run the K-S test between these trial data sets and the 22 μm -selected galaxies. For nearly all cases ($\sim 99.8\%$), the K-S test rejects the hypothesis that

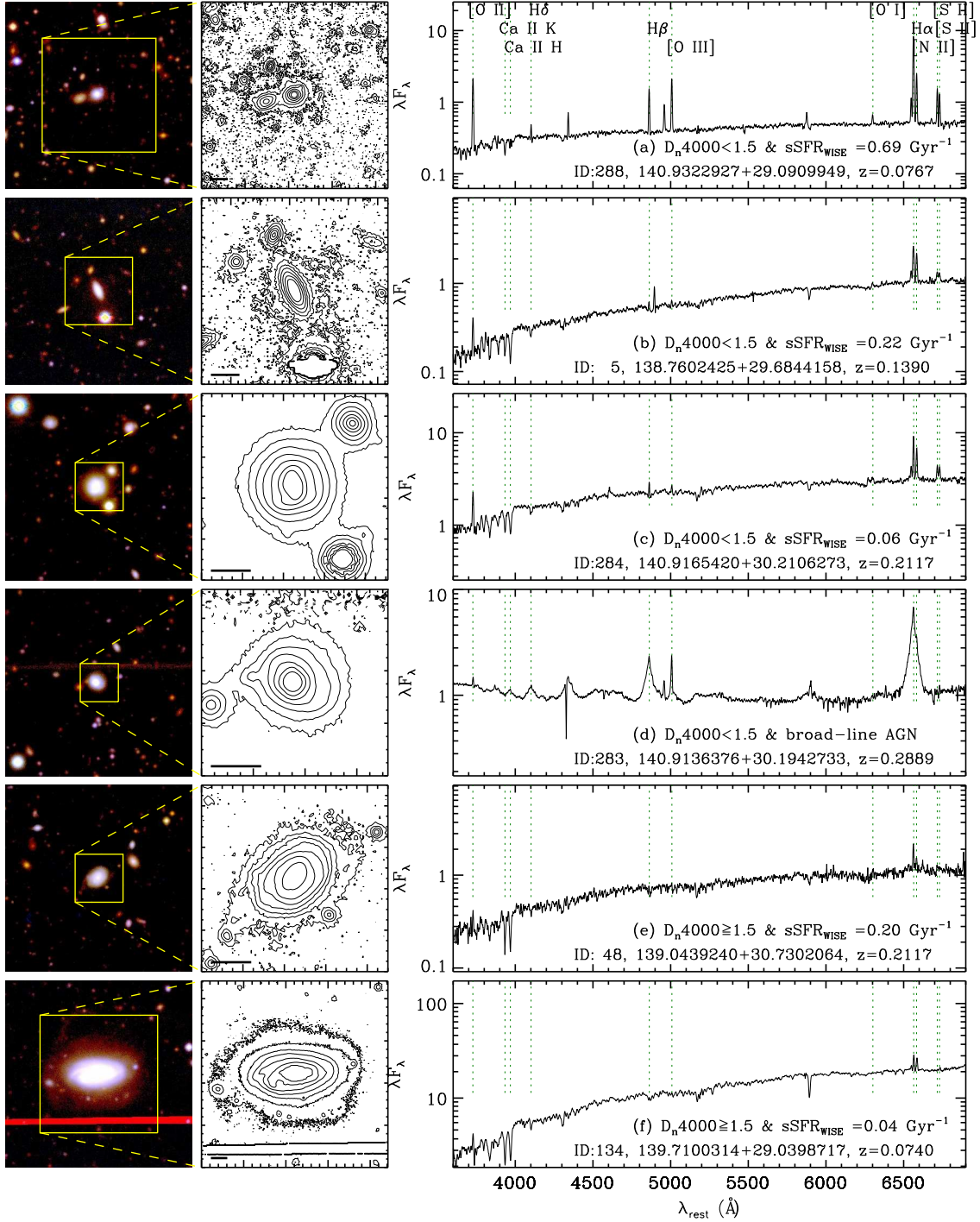


Figure 11. Example MMT spectra (right panels) with BVR color images ($90'' \times 90''$) (left panels) and R -band contour plots (middle panels) for $22 \mu\text{m}$ -selected galaxies. The north is up, and the east is to the left. The galaxy is marked by the square indicating the size, orientation and location of the contour plot in the color image. The contour plots centered on the optical counterparts represent the intensities in the R -band image. The size of each contour plot is $40 \text{ kpc} \times 40 \text{ kpc}$. The thick, horizontal bar represents 5 arcsec in each contour plot. The optical spectra are in unit of $10^{-17} \text{ erg s}^{-1} \text{ cm}^2$. ID, SHELs ID and redshift (see Table 2) of each source are shown.

the two distributions are extracted from the same parent population with a significance level of $> 99.7\%$, confirming that 22 μ m-selected galaxies are inconsistent with a random subsample of SHELS galaxies.

Panel (b) shows IR luminosities of 22 μ m-selected galaxies as a function of redshift. This figure clearly shows that the detection limit increases with redshift. LIRGs ($L_{IR} \geq 10^{11} L_{\odot}$) begin to appear at $z \approx 0.09$, and ULIRGs ($L_{IR} \geq 10^{12} L_{\odot}$) begin to appear at $z \approx 0.31$. At fixed redshift, the stellar masses of 22 μ m-selected galaxies are larger than those of 22 μ m-undetected galaxies (panel c). Similarly, the apparent R -band magnitudes of 22 μ m-selected galaxies are smaller than those of 22 μ m-undetected galaxies (panel d). Because there is a close connection between the stellar masses and the SFRs (i.e. IR luminosities) (e.g., Noeske et al. 2007; Elbaz et al. 2007), the larger masses (or small R -band magnitudes) of 22 μ m-selected galaxies result primarily from the IR detection limits in panel (b).

Panel (e) shows the flux ratio between $H\alpha$ and $H\beta$ (i.e. Balmer decrement) as a function of redshift. As expected, most 22 μ m-selected galaxies show $H\alpha/H\beta$ values larger than the intrinsic ratio in the nominal case B recombination for $T = 10,000$ K with no dust (i.e. $H\alpha/H\beta \sim 2.87$, Osterbrock & Ferland 2006). In the redshift range where both $H\alpha$ and $H\beta$ are measured (i.e. $z < 0.37$), the ratio does not change with redshift.

We show a sample of BVR color images, R -band contour plots, and optical spectra for 22 μ m-selected galaxies with various sSFRs and D_n4000 values in Figure 11. The figure shows a variety of spectral features depending on their sSFRs and D_n4000 . As expected, all of them have $H\alpha$ or [O II] emission lines, indicating their SF or nuclear activity. The other emission lines including $H\beta$ and [O III] are also strong for the galaxies with small D_n4000 (top four panels), but are very weak for those with large D_n4000 (bottom two panels). The Ca II H and K absorption lines, indicative of old stellar populations, are weak in the spectrum of the galaxy with the largest sSFR (a). These lines are not visible in the spectrum of the broad-line AGN (d). However, these lines are strong for the galaxies with large D_n4000 (bottom two panels).

3.2.2. Average Spectra

To examine the typical optical spectral features for 22 μ m-selected galaxies, we show the rest-frame median-stacked spectra of these galaxies binned in IR luminosity (Figure 12). Because LIRGs are distributed over a wide redshift range, we divide them into two subsamples based on their redshifts (i.e. $z < 0.2$ and $0.2 \leq z < 0.4$). We exclude the broad-line AGNs. Thanks to the wide wavelength coverage of Hectospec spectra, several spectral features including D_n4000 and the $H\alpha$ emission line are well represented for all subsamples. For example, many emission lines including [O II], [O III] and $H\alpha$ are clearly visible, indicating SF and/or nuclear activity. Higher-order Balmer absorption lines at < 3900 Å are also prominent for all subsamples. These lines are characteristic of short-lived ($\lesssim 1$ Gyr) A-type stars, typically present in post-starburst galaxies that may have experienced starbursts within the last Gyr but with no current SF (Dressler & Gunn 1983). However, we do not find any galaxies in our sample satisfying the selection criteria

for post-starburst galaxies (e.g., strong $H\delta$ absorption line and no [O II] and $H\alpha$ emission lines), probably because our samples are 22 μ m-selected galaxies that are still forming stars.

Some absorption lines including Na D and Ca II H and K, indicative of old stellar populations, are also visible in Figure 12 (see Caputi et al. 2008, 2009 for stacked spectra of *Spitzer* 24 μ m-selected galaxies at similar redshift for comparison). The comparison of stacked spectra among subsamples is interesting. As expected, $H\alpha$ and [O II] emission lines (SFR indicators) strengthen with increasing IR luminosity (from top to bottom). The strength of the [O III] line relative to $H\beta$ also grows with increasing IR luminosity, which can suggest an increase in nuclear activity.

To better demonstrate this trend of nuclear activity with IR luminosity, we plot the emission line ratios of [O III]/ $H\beta$ and [N II]/ $H\alpha$ for these stacked spectra in Figure 13. While the [N II]/ $H\alpha$ ratios do not change much with IR luminosity, the [O III]/ $H\beta$ ratios increase significantly with increasing IR luminosity. Although there are two LIRG samples at $z < 0.2$ and at $0.2 \leq z < 0.4$, the mean IR luminosity for LIRGs at $0.2 \leq z < 0.4$ slightly exceeds the mean IR luminosity of LIRGs at $z < 0.2$ ($\langle \log(L_{IR}) \rangle = 11.6$ vs. $= 11.1$) as a result of selection toward increasing luminosity limit with redshift (see Figure 10(b)). The number fraction of AGN-host galaxies in each subsample also increases with IR luminosity from 44% [$10 \leq \log(L_{IR}) < 11$] to 86% [$12 \leq \log(L_{IR})$], consistent with previous results (e.g., Veilleux et al. 1995, 2002; Yuan et al. 2010; Hwang et al. 2010a).

3.2.3. [Ne III] Strong Galaxies

During the visual inspection of all of the spectra of the 22 μ m-selected galaxies, we identified some unusual galaxies with strong emission lines not used for the line ratio diagram in Figure 7. These lines include [Ne III] 3869, 3968 Å (and sometimes He I 5876 Å) that require hard ionizing radiation such as AGN or extremely young massive stars (Osterbrock & Ferland 2006). To select these galaxies in an objective way, we use the equivalent widths (EWs) of [Ne III] 3869, 3968 Å lines: $EW_{[NeIII]3869} < -55$ Å and $EW_{[NeIII]3968} < -45$ Å. Among the 317 22 μ m-selected galaxies at $z < 0.8$, we find nine galaxies ($\sim 2.8\%$). This fraction is similar to the fractions of [Ne III] λ 3869, 3968 strong galaxies in SDSS (Shirazi & Brinchmann 2012, 1.2 – 2.7%). Reasonable changes in the selection criteria do not change the sample. Figure 14 shows the optical spectra along with optical color images and IDs (see Table 2).

The [Ne III] line is more conspicuous in AGNs than in star-forming galaxies (Rola et al. 1997). Actually, seven out of nine galaxies in our sample host AGNs. However, the hard radiation for [Ne III] line can also be provided by very young stars in HII regions (Shields 1990). There are two galaxies with SF class (see Figure 14). Moreover, many [Ne III] strong galaxies have large sSFRs (see Figure 15), suggesting that [Ne III] lines originate from SF as well as AGNs.

3.3. Correlation between specific SFRs and Optical Spectral Properties

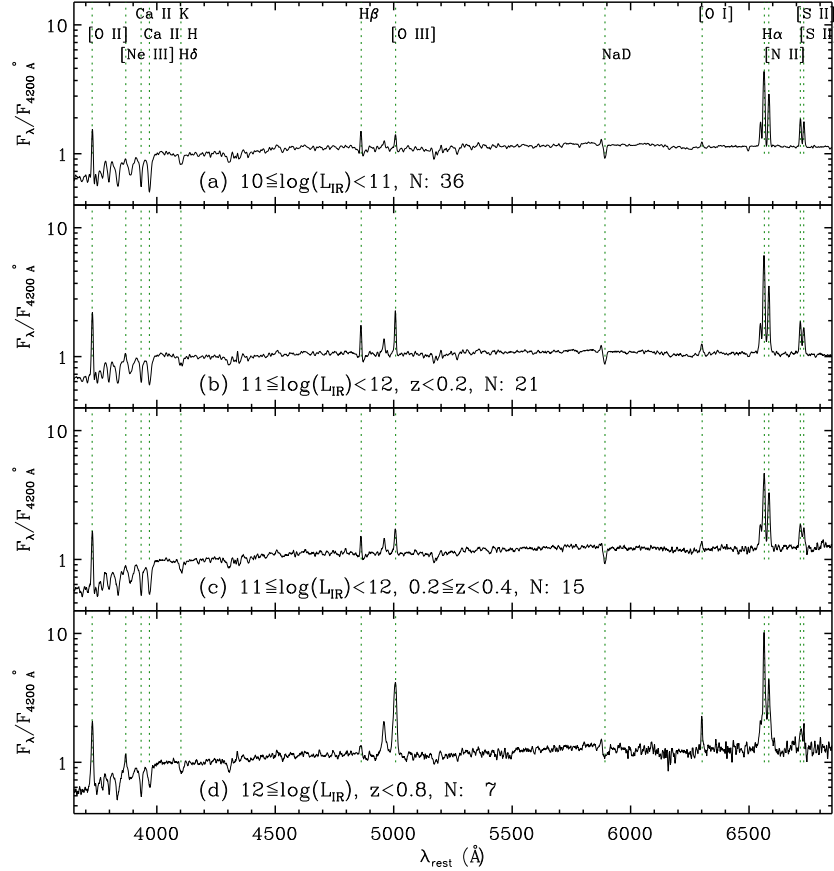


Figure 12. Stacked optical spectra of 22 μm -selected galaxies according to their IR luminosities and redshifts. N is the number of spectra in the stack.

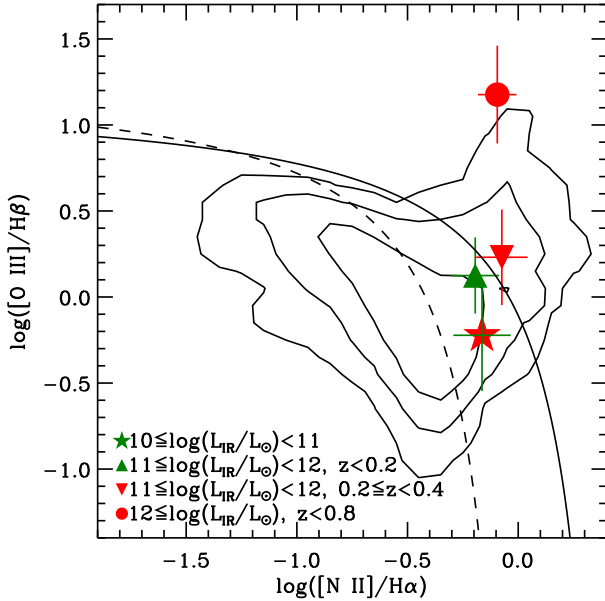


Figure 13. The line ratio diagram for the stacked spectra in Fig. 12. The solid and dashed lines in (a) indicate the extreme starbursts (Kewley et al. 2001) and pure SF limits (Kauffmann et al. 2003b), respectively. The contours indicate the distribution of all SHELs galaxies at $z < 0.37$ adopted from Fig. 7a.

To study how the SFA of 22 μm -selected galaxies evolves with cosmic time, we plot their sSFRs as a function of redshift in the left panel of Figure 15. The sSFRs of 22 μm -selected galaxies increase on average with red-

shift. We overplot the detection limit for galaxies with the largest stellar mass in our sample ($M_{\text{star}} \approx 3 \times 10^{12} M_{\odot}$) as a dotted line. The sSFRs of 22 μm -selected galaxies are much larger than the limit, suggesting that the increase of sSFRs with redshift is not strongly affected by the detection limit.

We overplot the mean evolutionary trend of IR-selected star-forming galaxies suggested by Elbaz et al. (2011, solid line). The *WISE* 22 μm -selected galaxies, on average, follow this evolutionary trend with some outliers with large sSFRs. Elbaz et al. introduced a “starburstness” parameter that is the ratio of sSFR of a galaxy to the median sSFR at a given redshift. Because this parameter corrects the underlying trend of sSFR with redshift, it is useful in making a fair comparison of the SFA of galaxies in a wide redshift range (e.g., $0 < z < 3$). However, the redshift range for our sample is small (most of galaxies relevant to the following analysis are at $z < 0.37$), and the slope of the evolutionary trend can differ depending on the sample selection (see Karim et al. 2011 and Elbaz et al. 2011 for detailed discussion on this issue including the slope of SFR- M_{star} relation). We thus simply use sSFR as a proxy for the SFA of galaxies for the following analysis. If we use the starburstness rather than sSFR, the results do not change.

Because H α bright galaxies are all detected at 22 μm , the general trend in Figure 15 does not change if we use H α luminosity rather than IR luminosity (see Westra et al. 2010 for the analysis based on H α luminosity). However, the H α fluxes can be easily contaminated

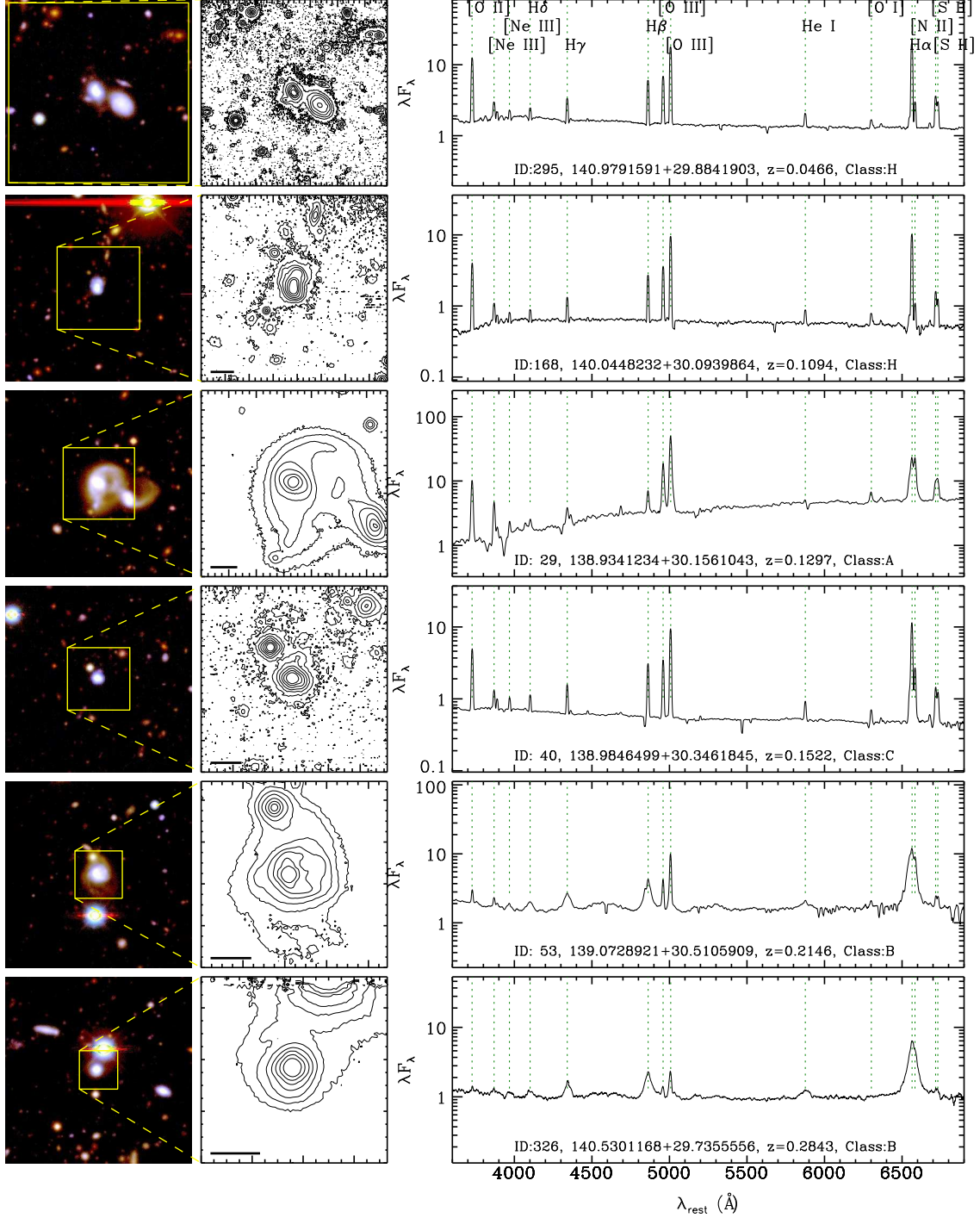


Figure 14. Same as Fig. 11, but for [Ne III] strong galaxies. For each source, we show ID, SHELS ID, redshift and SF/AGN classification in Table 2 (Class: H (SF), C (Composite), A (AGN from optical spectra), M (AGN from MIR colors), B (broad-line AGN)).

by the presence of AGN, they are often uncertain because of large extinction corrections for dusty galaxies, and they can not be measured for high- z galaxies because of the limited spectral coverage. The use of 22 μ m flux densities thus provides a more extensive view of SFA of galaxies.

The right panel of Figure 15 shows the sSFRs as a function of D_n4000 . As expected, the sSFRs of galaxies with small D_n4000 (e.g., < 1.2), on average, are larger than those with large D_n4000 (e.g., > 1.2). [Ne III] strong galaxies (crosses) in general have large sSFRs (e.g., $\gtrsim 0.4$

Gyr^{-1}), indicating their intense SFA.

There are some 22 μ m-selected galaxies with large D_n4000 (e.g., > 1.5), suggesting star formation in a system dominated by an old stellar population. Many of these objects are indeed morphologically early-type (with signs of disturbances in some cases). They show some emission lines in their optical spectra, indicating SF and/or nuclear activity (see Figure 11(e-f)). These galaxies are similar to star-forming (or blue), early-type galaxies found both in low- z and in high- z universe (e.g., Fukugita et al. 2004; Lee et al. 2006, 2010a; Hwang et al.

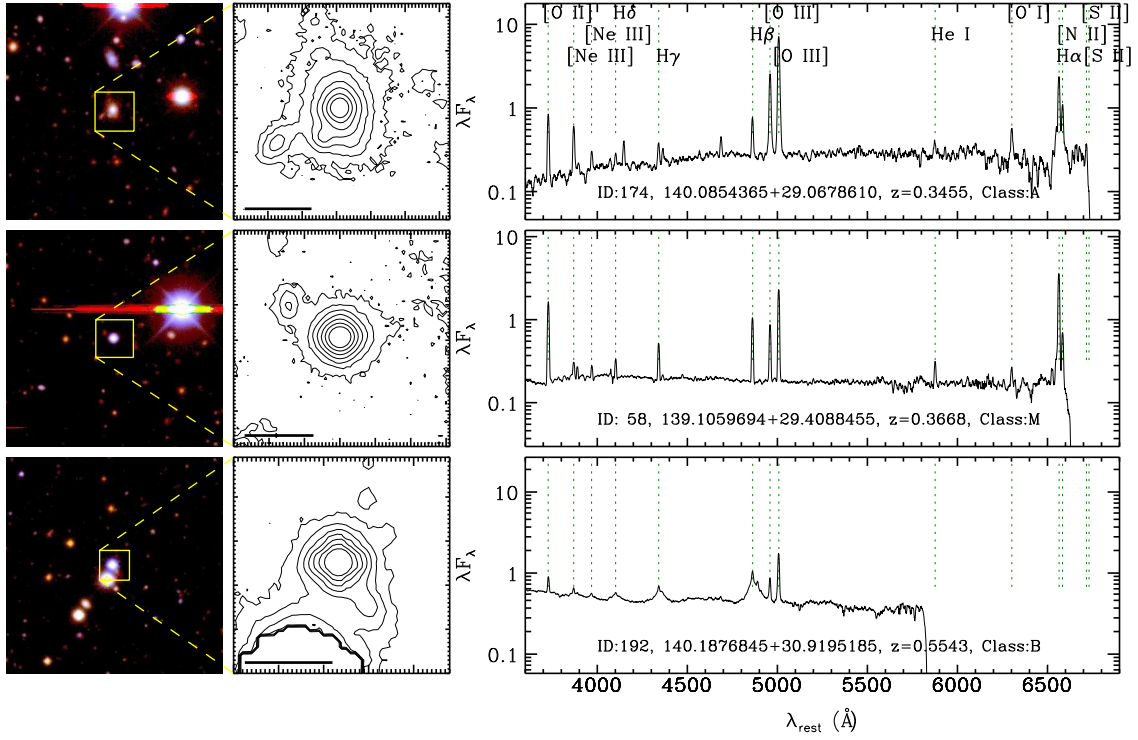


Fig. 14.— Continued

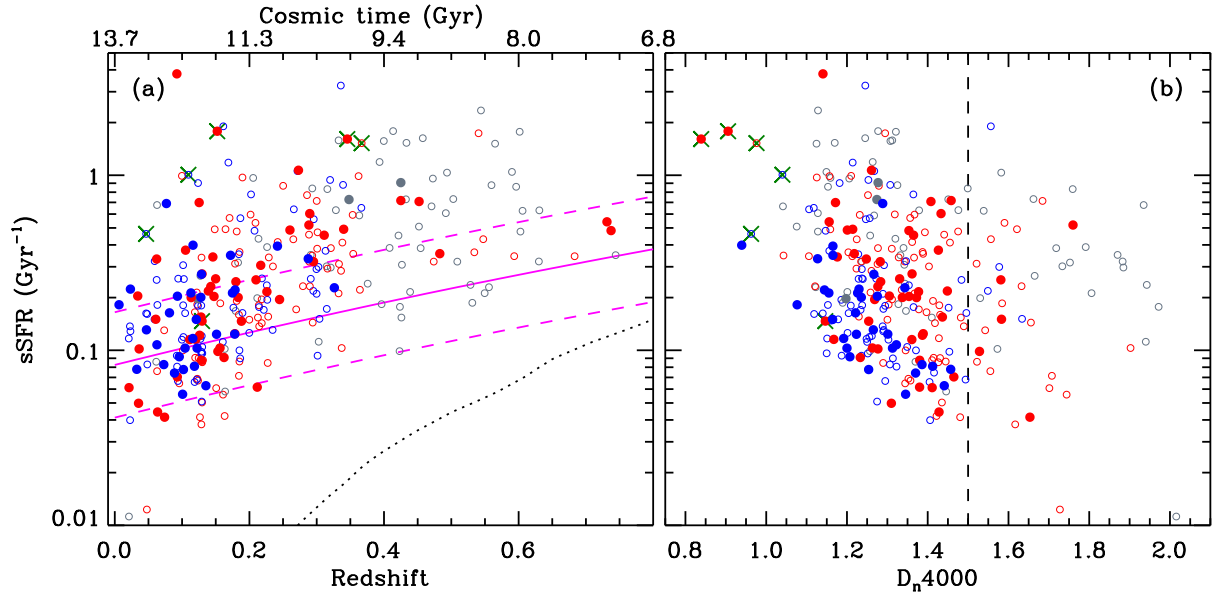


Figure 15. Redshift evolution of sSFRs of *WISE* 22 μm -selected galaxies (a). Filled and open symbols are galaxies with $S/N_{22\mu\text{m}} \geq 5$ and $S/N_{22\mu\text{m}} \geq 3$, respectively. Red and blue colors indicate AGN-host and SF galaxies, respectively, and gray colors are those without SF/AGN classification. The crosses are [Ne III] strong galaxies (see Section 3.2.3). The pink solid line is the median trend of normal SF galaxies in Elbaz et al. (2011). Two dashed lines indicate the boundaries for starburst and quiescent galaxies. The dotted line is the detection limit for galaxies with $M_{\text{star}} \approx 3 \times 10^{12} M_{\odot}$. (b) sSFRs vs. D_n4000 for *WISE* 22 μm -selected galaxies. Symbols are the same as in (a).

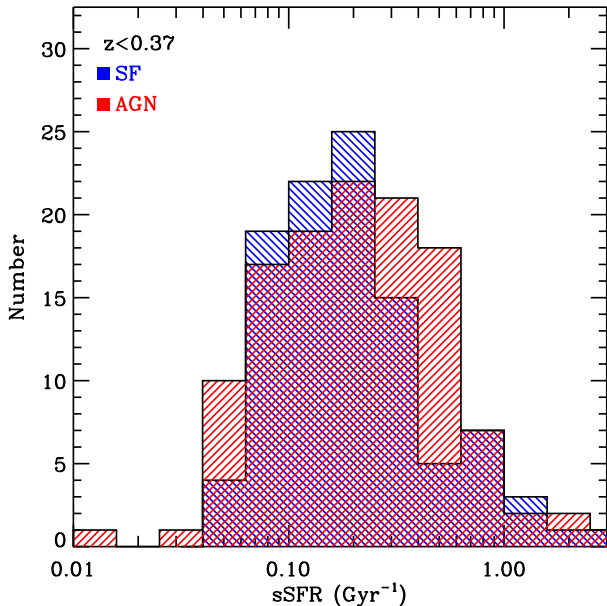


Figure 16. Distribution of sSFRs of the 22 μ m-selected galaxies with $S/N_{22\mu m} \geq 3$ depending on SF/AGN classification. Galaxies with AGN and SF classes at $z < 0.37$ are denoted by hatched histograms with orientation of 45° (// with red color) and of 315° (\\\ with blue color) relative to horizontal, respectively.

2012a); SF or nuclear activity probably results from recent galaxy interactions or mergers. We show the distribution of these objects in the optical line ratio (a) and *WISE* color-color (b) diagrams of Figure 7. There are a small number of galaxies satisfying the MIR AGN selection criteria. However, the *WISE* colors for the majority of these 22 μ m-selected galaxies with large D_n4000 (see panel b) are consistent with those of normal spiral galaxies: two galaxies are in the color range of elliptical galaxies. Among 38 22 μ m-selected galaxies with $D_n4000 > 1.5$ at $z < 0.37$, we can classify 24 galaxies based on the optical line ratios (panel a): 46%, 37% and 17% as AGN, composite and SF galaxies, respectively. The large fraction of AGN-host galaxies among the emission-line early-type galaxies is consistent with the results based on low- z galaxies (e.g., Schawinski et al. 2007; Lee et al. 2008). This large fraction can suggest that AGNs play a role in the evolution of emission-line early-type galaxies (Schawinski et al. 2007).

3.3.1. AGN vs. Star-forming Galaxies

The 22 μ m-selected galaxies are mostly SF galaxies, but they can also harbor AGNs. Here, we investigate the SFA of the 22 μ m-selected galaxies containing AGNs (see Section 2.4 for the description of AGN selection).

One interesting feature in the right panel of Figure 15 is that the sSFR distribution of AGN-host galaxies (red symbols) is not distinguishable from purely SF galaxies (blue symbols). To better demonstrate this coincidence, we compare the sSFR distribution of AGNs with that of SF galaxies in Figure 16. We use the galaxies (with $S/N_{22\mu m} \geq 3$) at $z < 0.37$ where we can classify them based on the optical spectra. The distribution of the two samples does not differ significantly. The K-S test rejects the hypothesis that the sSFR distribution of AGN and SF galaxies are extracted from the same parent population with only a significance level of 83%, suggesting the

similar underlying distribution of the two subsamples.

This result is consistent with the recent results in Mullaney et al. (2012), who showed that the majority of moderate luminosity X-ray AGNs at $0.5 < z < 3$ reside in normal SF galaxies (see also Santini et al. 2012 and Rovilos et al. 2012 for the most luminous X-ray AGNs). These results suggest that the nuclear activity in dusty star-forming galaxies at these redshifts is mainly fueled by internal processes (i.e. normal SF) rather than by violent mergers (i.e. starburst). Morphological analysis of AGN-host galaxies at high redshift also provides little evidence of recent merger events (e.g., Schawinski et al. 2011; Kocevski et al. 2012) in contrast with AGN-host galaxies in the local universe (e.g., Ellison et al. 2011; Hwang et al. 2012b).

3.3.2. Role of the Nearest Neighbor Galaxy in Changing sSFR

The SF or nuclear activity of galaxies is strongly affected by interactions with nearest neighbor galaxies (e.g., Barton et al. 2000; Woods et al. 2006; Geller et al. 2006; Ellison et al. 2008, 2011; Park & Choi 2009; Hwang et al. 2012b). To examine the role of neighbors in changing the SFA of galaxies, we show the sSFR distribution of the 22 μ m-selected galaxies depending on D_n4000 of their neighbors (i.e. D_n4000_{nei}) in the left panel of Figure 17.

To find the galaxies in potentially interacting pairs, we search for the nearest neighbor galaxy among galaxies with magnitudes brighter than $M_R = M_{R,target} + \Delta M_R$ and with relative velocities less than $\Delta v/(1+z) = |v_{neighbors} - v_{target}|/(1+z) = 500 \text{ km s}^{-1}$. Following Woods et al. (2010), we adopt $\Delta M_R = 1.75$, corresponding to a luminosity (or mass) ratio $> 1/5$. This criterion selects the galaxies in major interacting pairs; these objects should be the most effective in triggering SFA (Woods & Geller 2007; Cox et al. 2008; Hwang et al. 2010a). To have a fair sample of neighbor galaxies in our sample, we select the target galaxies among those with $m_R < (20.6 - 1.75)$ where $m_R = 20.6$ is the magnitude limit of SHELS. Because of this strict magnitude limit, the redshift range for the galaxies in this analysis is small ($z < 0.37$, see Figure 10d). The redshift effect on the change of sSFR is thus minimized.

We use $\Delta v/(1+z) = 500 \text{ km s}^{-1}$, the typical maximum velocity difference used for exploring close pairs in the local universe (see Fig. 2 of Barton et al. 2000 and Fig. 1 of Park et al. 2008). Because we are interested in the effect of neighbors interacting with target galaxies, we restrict our sample to close galaxy pairs with a projected spatial separation of $< 150 \text{ kpc}$. This separation is much smaller than the typical virial radius of late-type galaxies where galaxy properties begin to change because of galaxy interactions (e.g., $r_{vir} \approx 340 h_{70}^{-1} \text{ kpc}$ with $M_r = -20$, Park et al. 2008). There are 47 22 μ m-selected galaxies at $z < 0.37$ with close neighbors for the following analysis.

Panel (a) of Figure 17 shows that the peak sSFRs for galaxies with $D_n4000_{nei} < 1.5$ and > 1.5 are different. The median sSFR for galaxies with $D_n4000_{nei} \geq 1.5$ and $D_n4000_{nei} < 1.5$ is 0.12 ± 0.08 and 0.17 ± 0.09 , respectively. The K-S test rejects the hypothesis that two distributions are extracted from the same parent population with a significance level of 97%. Although the statistical

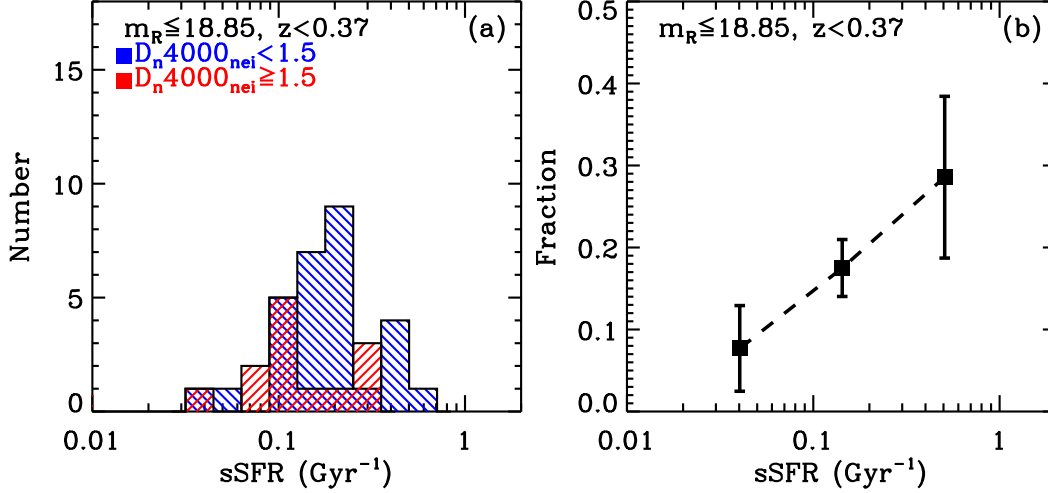


Figure 17. The sSFR distribution for the 22 μ m-selected galaxies with $S/N_{22\mu m} \geq 3$ depending on D_n4000 of the nearest neighbor galaxy (i.e. D_n4000_{nei}) (a). Galaxies with $D_n4000_{\text{nei}} \geq 1.5$ and $D_n4000_{\text{nei}} < 1.5$ are denoted by hatched histograms with orientation of 45° (// with red color) and of 315° (\ \ with blue color) relative to horizontal, respectively. The fraction of galaxies with close neighbors with $D_n4000_{\text{nei}} < 1.5$ among 22 μ m-selected ($S/N_{22\mu m} \geq 3$) galaxies as a function of sSFR (b). The associated errorbars indicate Poisson uncertainties.

significance is not very high, this result can be consistent with the results that interactions between gas-rich galaxies (i.e. $D_n4000_{\text{nei}} < 1.5$) increase the SFRs; interactions involving gas-poor galaxies (i.e. $D_n4000_{\text{nei}} \geq 1.5$) do not (e.g., Woods & Geller 2007; Park & Choi 2009; Xu et al. 2010). This trend is also seen even for FIR-selected galaxies both in low- z and in high- z universe (Hwang et al. 2010a, 2011).

Figure 17(b) shows the fraction of 22 μ m-selected galaxies with projected close neighbors with $D_n4000_{\text{nei}} < 1.5$ as a function of sSFR. The fraction of galaxies with close neighbors clearly increases with sSFR. This dependence strongly supports the idea that the sSFRs of galaxies with close neighbors in this redshift range ($z < 0.37$) are indeed enhanced by the interactions with gas-rich ($D_n4000 < 1.5$) galaxies (e.g., Woods & Geller 2007; Woods et al. 2010; Hwang et al. 2011).

Among the six [Ne III] strong galaxies in this redshift range, only one galaxy has a close neighbor (ID 29). If the large SFRs of these objects result from very recent galaxy interactions or mergers, this result suggests that they are in the late stage of merging; when two galaxies merge, the new nearest neighbor galaxy of the merger product may be far away. The optical images for some of these objects show signs of tidal disturbances (see Figure 14), supporting this suggestion that they are merger remnants. An extensive analysis of the morphology of these objects along with nearby analogs (e.g., Shirazi & Brinchmann 2012) and a larger sample would clarify this issue.

4. CONCLUSIONS

Using a dense redshift survey (SHELS) covering a 4 square degree region of a deep imaging survey (DLS), we obtain a nearly complete identification of optical counterparts of *WISE* 22 μ m sources. The properties of the *WISE*-selected sample are:

1. Among 507 *WISE* 22 μ m sources with $(S/N)_{22\mu m} \geq 3$ ($\approx S_{22\mu m} \gtrsim 2.5$ mJy) in the SHELS field, we identify 481 sources with optical counterparts in the very deep, DLS R -band source

catalog (down to $R < 25.2$). There are 337 galaxies at $R < 21$ with spectroscopic data.

2. The 22 μ m-selected galaxies are dusty star-forming galaxies with young stellar populations (i.e. small D_n4000). Most of them are at $z < 0.8$ with a median redshift of $\langle z \rangle = 0.2$. Their IR luminosities are in the range $4.5 \times 10^8 (L_\odot) \lesssim L_{IR} \lesssim 7.8 \times 10^{12} (L_\odot)$ with a median L_{IR} of $1.3 \times 10^{11} (L_\odot)$.
3. There are some ($\sim 14\%$) 22 μ m-selected galaxies with large D_n4000 (> 1.5), indicating star formation and/or nuclear activity in a system dominated by an old stellar population. Many of these objects with emission lines in their optical spectra are classified as AGN-host galaxies, suggesting that AGNs may play a role in the evolution of these objects.

Thanks to the wavelength coverage of Hectospec spectra, we identify several interesting features from the optical spectra of the 22 μ m-selected galaxies:

1. The stacked spectra binned in IR luminosity show that the strength of the [O III] line relative to H β grows with increasing IR luminosity, which can suggest an increase in nuclear activity with IR luminosity.
2. We identify nine unusual galaxies with very strong [Ne III] $\lambda 3869$, 3968 emission lines (i.e. $EW_{[\text{NeIII}]\lambda 3869} < -55 \text{ \AA}$ and $EW_{[\text{NeIII}]\lambda 3968} < -45 \text{ \AA}$). AGN and/or extremely young stars can produce this emission.

We also study the effects of the presence of AGNs and of the nearest neighbor galaxy on the change in sSFRs of the 22 μ m-selected galaxies:

1. The sSFR distribution of AGN-host galaxies is similar to pure SF galaxies, indicating the coexistence of SF and AGN.

2. The sSFRs of 22 μ m-selected galaxies with late-type neighbors appear to be larger than those with early-type neighbors. The fraction of galaxies with close neighbors increases with sSFR. These results suggest an important role of the nearest neighbor galaxies in changing the SFA of galaxies.

The combination of *WISE* data with very deep, optical photometric data provides a large sample of dusty galaxies; we identify 48 DOG candidates with large MIR to optical flux density ratios (i.e. $S_{22\mu\text{m}}/S_{0.65\mu\text{m}} \geq 982$). None of these objects have SHELS spectroscopic data. Ten of them have no optical counterparts even in the very deep, DLS *R*-band source catalog.

Remarkably, *WISE* data probe the universe to $z \sim 2$ (e.g., DOGs). We identify these high- z objects based on the very deep, DLS optical photometric data. The SHELS dense spectroscopic survey data elucidate the spectroscopic properties of the *WISE* sources at $z \lesssim 0.8$. To explore the nature of *WISE* sources further, we plan to investigate other fields including HectoMAP and DLS F1 field where there are extensive data sets including deep optical photometry, dense redshift survey data, and uniform *WISE* photometry.

We thank the anonymous referee for his/her useful comments that improved the original manuscript. We thank Scott Kenyon for carefully reading the manuscript and Jong Chul Lee for useful discussion. HSH acknowledges the Smithsonian Institution for the support of his post-doctoral fellowship. The Smithsonian Institution also supports the research of MJG, MJK and DGF. IPD is supported by NSF-AST grant AST-0708433. Observations reported here were obtained at the MMT Observatory, a joint facility of the Smithsonian Institution and the University of Arizona. This research has made use of the NASA/IPAC Infrared Science Archive, which is operated by the Jet Propulsion Laboratory, California Institute of Technology, under contract with the National Aeronautics and Space Administration. This publication makes use of data products from the Wide-field Infrared Survey Explorer, which is a joint project of the University of California, Los Angeles, and the Jet Propulsion Laboratory/California Institute of Technology, funded by the National Aeronautics and Space Administration.

REFERENCES

- Alexander, D. M., & Hickox, R. C. 2012, *New Astron. Rev.*, 56, 93
- Assef, R. J., Kochanek, C. S., Brodwin, M., et al. 2010, *ApJ*, 713, 970
- Baldwin, J. A., Phillips, M. M., & Terlevich, R. 1981, *PASP*, 93, 5
- Balogh, M. L., Morris, S. L., Yee, H. K. C., Carlberg, R. G., & Ellingson, E. 1999, *ApJ*, 527, 54
- Barton, E. J., Geller, M. J., & Kenyon, S. J. 2000, *ApJ*, 530, 660
- Berta, S., Fritz, J., Franceschini, A., Bressan, A., & Pernechele, C. 2003, *A&A*, 403, 119
- Brinchmann, J., Charlot, S., White, S. D. M., et al. 2004, *MNRAS*, 351, 1151
- Bruzual, A. G. 1983, *ApJ*, 273, 105
- Bruzual, G., & Charlot, S. 2003, *MNRAS*, 344, 1000
- Calzetti, D., Armus, L., Bohlin, R. C., et al. 2000, *ApJ*, 533, 682
- Cao, C., Wu, H., Wang, J.-L., et al. 2006, *Chin. J. Astron. Astrophys.*, 6, 197
- Caputi, K. I., Lilly, S. J., Aussel, H., et al. 2008, *ApJ*, 680, 939
- . 2009, *ApJ*, 707, 1387
- Chary, R., & Elbaz, D. 2001, *ApJ*, 556, 562
- Colless, M., Dalton, G., Maddox, S., et al. 2001, *MNRAS*, 328, 1039
- Cox, T. J., Jonsson, P., Somerville, R. S., Primack, J. R., & Dekel, A. 2008, *MNRAS*, 384, 386
- Daddi, E., Dickinson, M., Morrison, G., et al. 2007, *ApJ*, 670, 156
- Dariush, A., Cortese, L., Eales, S., et al. 2011, *MNRAS*, 418, 64
- de Lapparent, V., Geller, M. J., & Huchra, J. P. 1986, *ApJ*, 302, L1
- Dey, A., Soifer, B. T., Desai, V., et al. 2008, *ApJ*, 677, 943
- Donoso, E., Yan, L., Tsai, C., et al. 2012, *ApJ*, 748, 80
- Draine, B. T., Dale, D. A., Bendo, G., et al. 2007, *ApJ*, 663, 866
- Dressler, A., & Gunn, J. E. 1983, *ApJ*, 270, 7
- Driver, S. P., Hill, D. T., Kelvin, L. S., et al. 2011, *MNRAS*, 413, 971
- Elbaz, D., Daddi, E., Le Borgne, D., et al. 2007, *A&A*, 468, 33
- Elbaz, D., Hwang, H. S., Magnelli, B., et al. 2010, *A&A*, 518, L29
- Elbaz, D., Dickinson, M., Hwang, H. S., et al. 2011, *A&A*, 533, 119
- Ellison, S. L., Patton, D. R., Mendel, J. T., & Scudder, J. M. 2011, *MNRAS*, 418, 2043
- Ellison, S. L., Patton, D. R., Simard, L., & McConnachie, A. W. 2008, *AJ*, 135, 1877
- Fabian, A. C. 2012, *ARA&A*, in press (arXiv:1204.4114)
- Fabricant, D., Fata, R., Roll, J., et al. 2005, *PASP*, 117, 1411
- Fabricant, D. G., Kurtz, M. J., Geller, M. J., et al. 2008, *PASP*, 120, 1222
- Flagey, N., Boulanger, F., Verstraete, L., et al. 2006, *A&A*, 453, 969
- Fukugita, M., Nakamura, O., Turner, E. L., Helmboldt, J., & Nichol, R. C. 2004, *ApJ*, 601, L127
- Geller, M. J., Dell’Antonio, I. P., Kurtz, M. J., et al. 2005, *ApJ*, 635, L125
- Geller, M. J., Diaferio, A., Kurtz, M. J., Dell’Antonio, I. P., & Fabricant, D. G. 2012, *AJ*, 143, 102
- Geller, M. J., & Huchra, J. P. 1989, *Science*, 246, 897
- Geller, M. J., Kenyon, S. J., Barton, E. J., Jarrett, T. H., & Kewley, L. J. 2006, *AJ*, 132, 2243
- Geller, M. J., Kurtz, M. J., Dell’Antonio, I. P., Ramella, M., & Fabricant, D. G. 2010, *ApJ*, 709, 832
- Genzel, R., & Cesarsky, C. J. 2000, *ARA&A*, 38, 761
- Goto, T. 2005, *MNRAS*, 360, 322
- Goto, T., Arnouts, S., Malkan, M., et al. 2011, *MNRAS*, 414, 1903
- Gott, III, J. R., Jurić, M., Schlegel, D., et al. 2005, *ApJ*, 624, 463
- Hancock, M., Smith, B. J., Struck, C., et al. 2007, *AJ*, 133, 676
- Hou, L. G., Wu, X.-B., & Han, J. L. 2009, *ApJ*, 704, 789
- Huchra, J., Davis, M., Latham, D., & Tonry, J. 1983, *ApJS*, 52, 89
- Hwang, H. S., Elbaz, D., Lee, J. C., et al. 2010a, *A&A*, 522, 33
- Hwang, H. S., Geller, M. J., Diaferio, A., & Rines, K. J. 2012a, *ApJ*, 752, 64
- Hwang, H. S., Park, C., Elbaz, D., & Choi, Y.-Y. 2012b, *A&A*, 538, 15
- Hwang, H. S., Serjeant, S., Lee, M. G., Lee, K. H., & White, G. J. 2007, *MNRAS*, 375, 115
- Hwang, H. S., Elbaz, D., Magdis, G., et al. 2010b, *MNRAS*, 409, 75
- Hwang, H. S., Elbaz, D., Dickinson, M., et al. 2011, *A&A*, 535, 60
- Isobe, T., Feigelson, E. D., Akritas, M. G., & Babu, G. J. 1990, *ApJ*, 364, 104
- Jarrett, T. H., Cohen, M., Masci, F., et al. 2011, *ApJ*, 735, 112
- Jones, D. H., Saunders, W., Colless, M., et al. 2004, *MNRAS*, 355, 747
- Karim, A., Schinnerer, E., Martínez-Sansigre, A., et al. 2011, *ApJ*, 730, 61
- Kartaltepe, J. S., Sanders, D. B., Le Floc’h, E., et al. 2010, *ApJ*, 721, 98
- Kartaltepe, J. S., Dickinson, M., Alexander, D. M., et al. 2011, *ApJ*, submitted (arXiv:1110.4057)
- Kauffmann, G., Heckman, T. M., White, S. D. M., et al. 2003a, *MNRAS*, 341, 33
- Kauffmann, G., Heckman, T. M., Tremonti, C., et al. 2003b, *MNRAS*, 346, 1055
- Kennicutt, Jr., R. C. 1998, *ARA&A*, 36, 189
- Kennicutt, Jr., R. C., & Evans, II, N. J. 2012, *ARA&A*, in press (arXiv:1204.3552)

- Kewley, L. J., Dopita, M. A., Sutherland, R. S., Heisler, C. A., & Trevena, J. 2001, *ApJ*, 556, 121
- Ko, J., Im, M., Lee, H. M., et al. 2012, *ApJ*, 745, 181
- Kocevski, D. D., Faber, S. M., Mozena, M., et al. 2012, *ApJ*, 744, 148
- Kroupa, P. 2001, *MNRAS*, 322, 231
- Lake, S. E., Wright, E. L., Petty, S., et al. 2012, *AJ*, 143, 7
- Lee, J. C., Hwang, H. S., Lee, M. G., Kim, M., & Kim, S. C. 2011, *MNRAS*, 414, 702
- Lee, J. C., Hwang, H. S., Lee, M. G., Kim, M., & Lee, J. H. 2012, *ApJ*, in press (arXiv:1207.1816)
- Lee, J. H., Hwang, H. S., Lee, M. G., Lee, J. C., & Matsuhara, H. 2010a, *ApJ*, 719, 1946
- Lee, J. H., Lee, M. G., & Hwang, H. S. 2006, *ApJ*, 650, 148
- Lee, J. H., Lee, M. G., Park, C., & Choi, Y.-Y. 2008, *MNRAS*, 389, 1791
- . 2010b, *MNRAS*, 401, 1804
- Lin, Y.-T., Stanford, S. A., Eisenhardt, P. R. M., et al. 2012, *ApJ*, 745, L3
- Lu, N., Helou, G., Werner, M. W., et al. 2003, *ApJ*, 588, 199
- Lutz, D., Poglitsch, A., Altieri, B., et al. 2011, *A&A*, 532, A90
- Magdis, G. E., Rigopoulou, D., Huang, J., & Fazio, G. G. 2010, *MNRAS*, 401, 1521
- Magnelli, B., Chary, R. R., Pope, A., et al. 2008, *ApJ*, 681, 258
- McKee, C. F., & Ostriker, E. C. 2007, *ARA&A*, 45, 565
- Mullaney, J. R., Pannella, M., Daddi, E., et al. 2012, *MNRAS*, 419, 95
- Murakami, H., Baba, H., Barthel, P., et al. 2007, *PASJ*, 59, 369
- Neugebauer, G., Habing, H. J., van Duinen, R., et al. 1984, *ApJ*, 278, L1
- Noeske, K. G., Weiner, B. J., Faber, S. M., et al. 2007, *ApJ*, 660, L43
- Oliver, S. J., Bock, J., Altieri, B., et al. 2012, *MNRAS*, 424, 1614
- Osterbrock, D. E., & Ferland, G. J. 2006, *Astrophysics of gaseous nebulae and active galactic nuclei*, ed. Osterbrock, D. E. & Ferland, G. J.
- Pannella, M., Carilli, C. L., Daddi, E., et al. 2009, *ApJ*, 698, L116
- Park, C., & Choi, Y. 2009, *ApJ*, 691, 1828
- Park, C., Gott, J. R. I., & Choi, Y. 2008, *ApJ*, 674, 784
- Park, C., & Hwang, H. S. 2009, *ApJ*, 699, 1595
- Penner, K., et al. 2012, *ApJ*, submitted
- Pilbratt, G. L., Riedinger, J. R., Passvogel, T., et al. 2010, *A&A*, 518, L1
- Polletta, M., Tajer, M., Maraschi, L., et al. 2007, *ApJ*, 663, 81
- Rola, C. S., Terlevich, E., & Terlevich, R. J. 1997, *MNRAS*, 289, 419
- Rovilos, E., Comastri, A., Gilli, R., et al. 2012, *A&A*, in press (arXiv:1207.7129)
- Salpeter, E. E. 1955, *ApJ*, 121, 161
- Sanders, D. B., & Mirabel, I. F. 1996, *ARA&A*, 34, 749
- Santini, P., Rosario, D. J., Shao, L., et al. 2012, *A&A*, 540, 109
- Schawinski, K., Thomas, D., Sarzi, M., et al. 2007, *MNRAS*, 382, 1415
- Schawinski, K., Treister, E., Urry, C. M., et al. 2011, *ApJ*, 727, L31
- Shields, G. A. 1990, *ARA&A*, 28, 525
- Shirazi, M., & Brinchmann, J. 2012, *MNRAS*, 421, 1043
- Soifer, B. T., Helou, G., & Werner, M. 2008, *ARA&A*, 46, 201
- Veilleux, S., Kim, D., & Sanders, D. B. 2002, *ApJS*, 143, 315
- Veilleux, S., Kim, D., Sanders, D. B., Mazzarella, J. M., & Soifer, B. T. 1995, *ApJS*, 98, 171
- Veilleux, S., & Osterbrock, D. E. 1987, *ApJS*, 63, 295
- Veilleux, S., Rupke, D. S. N., Kim, D., et al. 2009, *ApJS*, 182, 628
- Wang, L., & Rowan-Robinson, M. 2009, *MNRAS*, 398, 109
- Westra, E., Geller, M. J., Kurtz, M. J., Fabricant, D. G., & Dell’Antonio, I. 2010, *ApJ*, 708, 534
- Wittman, D., Dell’Antonio, I. P., Hughes, J. P., et al. 2006, *ApJ*, 643, 128
- Wittman, D. M., Tyson, J. A., Dell’Antonio, I. P., et al. 2002, in *Society of Photo-Optical Instrumentation Engineers (SPIE) Conference Series*, ed. J. A. Tyson & S. Wolff, Vol. 4836, 73–82
- Woods, D. F., & Geller, M. J. 2007, *AJ*, 134, 527
- Woods, D. F., Geller, M. J., & Barton, E. J. 2006, *AJ*, 132, 197
- Woods, D. F., Geller, M. J., Kurtz, M. J., et al. 2010, *AJ*, 139, 1857
- Wright, E. L., Eisenhardt, P. R. M., Mainzer, A. K., et al. 2010, *AJ*, 140, 1868
- Xu, C. K., Domingue, D., Cheng, Y., et al. 2010, *ApJ*, 713, 330
- York, D. G., Adelman, J., Anderson, Jr., J. E., et al. 2000, *AJ*, 120, 1579
- Yuan, T., Kewley, L. J., & Sanders, D. B. 2010, *ApJ*, 709, 884